Molecular density-accelerated binding-site maturation underlies CENP-T-dependent kinetochore assembly

Ekaterina V. Tarasovetc[1], Gunter B. Sissoko[2,3], Anna S. Mukhina[4], Aleksandr Maiorov[1], Fazoil I. Ataullakhanov[5-7], Iain M. Cheeseman[2,3], Ekaterina L. Grishchuk[1]*

[1] Department of Physiology, Perelman School of Medicine, University of Pennsylvania; Philadelphia, PA 19104, USA.

[2] Whitehead Institute for Biomedical Research; Cambridge, MA 02142, USA.

[3] Department of Biology, Massachusetts Institute of Technology; Cambridge, MA 02142, USA.

[4] Department of Physics, Lomonosov Moscow State University; Moscow, 119991, Russia.

[5] Center for Theoretical Problems of Physicochemical Pharmacology, Russian Academy of Sciences; Moscow, 119991, Russia.

[6] Dmitry Rogachev National Research Center of Pediatric Hematology, Oncology and Immunology; Moscow, 117198, Russia.

[7] Moscow Institute of Physics and Technology; 141701, Dolgoprudny, Russia.

*Corresponding author: Ekaterina L. Grishchuk

Email: gekate@pennmedicine.upenn.edu

Abstract

Formation of macromolecular cellular structures relies on recruitment of multiple proteins, requiring the precisely controlled pairwise binding interactions. At human kinetochores, our recent work found that the high molecular density environment enables strong bonding between the Ndc80 complex and its two binding sites at the CENP-T receptor. However, the mechanistic basis for this unusual density-dependent facilitation remains unknown. Here, using quantitative single-molecule approaches, we reveal two distinct mechanisms that drive preferential recruitment of the Ndc80 complex to higher-order structures of CENP-T, as opposed to CENP-T monomers. First, the Ndc80 binding sites within the disordered tail of the CENP-T mature over time, leading to a stronger grip on the Spc24/25 heads of the Ndc80 complexes. Second, the maturation of Ndc80 binding sites is accelerated when CENP-T molecules are clustered in close proximity. The rates of the clustering-induced maturation are remarkably different for two binding sites within CENP-T, correlating with different interfaces formed by the corresponding CENP-T sequences as they wrap around the Spc24/25 heads. The differential clustering-dependent regulation of these sites is preserved in dividing human cells, suggesting a distinct regulatory entry point to control kinetochore-microtubule interactions. The tunable acceleration of slowly maturing binding sites by a high molecular-density environment may represent a fundamental physicochemical mechanism to assist the assembly of mitotic kinetochores and other macromolecular structures.

Main Text

Introduction

During the biogenesis of higher-order cellular assemblies, hundreds of protein complexes and their subunits must come together from the crowded cellular milieu to build robust structures on biologically relevant timescales. However, how the binding of individual soluble components is directed specifically to the assembling structures, while preventing the same components from forming potentially toxic and wasteful complexes in the cytosol, remains unclear. Some highly stable multimolecular structures, including viral particles, assemble in a modular manner, with individual subunits engaging in direct interactions only during the initial assembly stages. These initial subcomplexes subsequently oligomerize and mature via posttranslational modifications, targeted proteolysis, and chaperone activities, which collectively ensure formation of the complete final structures (1). In contrast, the formation of mitotic kinetochores, which consist of multiple copies for more than 100 different proteins, is thought to involve a hierarchical array of direct binding reactions between individual components.

Different kinetochore components are recruited via pair-wise interactions in a defined temporal order to form a dense mesoscale meshwork (2). Human kinetochores contain approximately 70 copies of the scaffolding protein CENP-T, which is present in a cytosolic fraction at a concentration of 5-25 nM (3-5). The kinetochore-associated CENP-T directly recruits Ndc80 protein complexes from its 50-150 nM cytosolic pool (2-7). To sustain forces during chromosome segregation, Ndc80 must bond with CENP-T via a high-affinity interface (8), implying that these interactions are not reversible at physiological timescale. Thus, specific molecular mechanisms must ensure that the Ndc80 and CENP-T scaffold avoid binding in a soluble pool, while permitting their bonding at the kinetochore.

Several mechanisms have been proposed to assist binding interactions at the assembling kinetochores, including mitosis-specific phosphorylation (9-16), autoinhibition (12, 17-20), and nuclear-cytoplasmic compartmentalization (9). However, these regulatory mechanisms fail to explain our recent findings in mitotic human cells that formation of Ndc80-CENP-T complexes depends on their specific molecular environment (21). Indeed, the disordered N-terminus of CENP-T, which contains two Ndc80 binding sites (5, 10, 22-24), recruits Ndc80 poorly in mitotic cytoplasm, suggesting weak Ndc80 binding affinity. Strikingly, in cells, artificially-generated CENP-T multimers with the same CENP-T protein levels recruit Ndc80 efficiently, implying that CENP-T molecules in a clustered form have a stronger binding affinity for Ndc80 (21). However, the molecular mechanisms that bias Ndc80 binding to the high-density clusters of CENP-T remain unclear, necessitating quantitative and rigorous biochemical and biophysical studies to define the kinetics of these reactions.

The classical paradigm of protein-protein interactions involves single-step binding and dissociation of interactors, with the steady-state fraction of components in a complex determined by the ratio of the corresponding rate constants. Within this framework, the steady-state number of Ndc80 molecules bound to one CENP-T molecule does not depend on the molecular density of CENP-T (given the same total number of CENP-T molecules). However, many pairwise interactions involving proteins with unstructured regions proceed with multi-step binding kinetics, often generating multiple complexes with different binding affinities (25, 26). Furthermore, the density of molecular environment formed by unstructured proteins may modulate such intricate interactions, giving rise emergent properties at sites where molecules are clustered. Prompted by these hypotheses, we sought to determine the mechanisms of density-dependent changes in affinity of Ndc80-CENP-T complexes *in vitro* and to probe these kinetic relationships within the cellular environment. Our work reveals an elegant regulatory mechanism involving a density-dependent kinetic barrier for the maturation of individual Ndc80 binding sites in the disordered N-terminus of the CENP-T protein.

Results

Initial Ndc80 binding by CENP-T monomers is unstable but Ndc80 retention increases over time

We first analyzed the behavior of a CENP-T N-terminal fragment activated with phosphomimetic substitutions by immobilizing these molecules at low density on a coverslip in a flow chamber (Fig. 1A). Using total internal reflection fluorescence (TIRF) microscopy, we monitored the brightness of CENP-T^{6D} monomers in the presence of soluble GFP-tagged Ndc80 complex using an internally truncated "Bonsai" protein ((27); thereafter called Ndc80 complex) (Fig. 1B,C; *SI Appendix*, Fig. S1E). At 200 nM Ndc80 complex, which is comparable to the intracellular Ndc80 concentration (3, 4), binding of Ndc80 to CENP-T monomers was fast, plateauing at roughly two Ndc80 molecules per CENP-T^{6D} (Fig. 1D). In contrast, this same assay did not detect binding between CENP-T^{6D} and an Ndc80 construct lacking its CENP-T binding domain (Ndc80 ΔSpc24/25).

To probe the stability of Ndc80-CENP-T complexes, we abruptly removed soluble Ndc80 after a 10 min incubation by washout. Ndc80 dissociation kinetics were bi-phasic, with most Ndc80 detaching immediately, but ~30% remaining as a stable population (Fig. 1E). Since both Ndc80 complex binding sites on CENP-T achieve steady-state binding within ~ 1 min (Fig. 1D), washout of the Ndc80 complex at any time point after saturation should result in a similar disassociation from CENP-T. Strikingly, although Ndc80 dissociation kinetics at later time points remained bi-phasic, the fraction of the stably bound Ndc80s increased progressively, reaching ~ 60% when interactions were allowed to occur for 60 min prior to washout (Fig. 1F). This result could not be explained by changes in CENP-T alone, because the stability of Ndc80 binding to CENP-T remained the same when CENP-T was incubated with a buffer alone for an extended time prior to Ndc80 addition (*SI Appendix,* Fig. S2A, Note 1, section 1). The increased binding stability also could not be attributed to the binding of additional Ndc80 molecules, because the total number of bound Ndc80 molecules remained close to 2 during the entire experiment (Fig. 1F,G). In contrast, in a similar assay, complexes between GFP and its nanobody (GBP) were highly stable and did not change based on incubation time (Fig. 1E). Thus, although monomeric CENP-T^{6D} binds to Ndc80 rapidly, an extended interaction time is needed to develop high-affinity bonding between these proteins. Under the tested conditions, high-affinity binding of two Ndc80 molecules was not achieved even after 60 min, exceeding the time required for chromosome segregation.

The Ndc80 binding sites in CENP-T have similar affinities, but differing maturation rates

The enhanced retention of Ndc80 after saturation of binding sites strongly implies that, upon Ndc80 association, the sites change their molecular properties. CENP-T contains two distinct binding sites for Ndc80 (10, 22, 23). Structural analysis of the Ndc80 binding sites in CENP-T using AlphaFold2 predictions revealed substantial differences in their 3D configurations, manifesting in a different extent of wrapping around the Spc24/25 head of the Ndc80 protein (Fig. 2A; *SI Appendix,* Figs. S3, S4, Note 2). To test whether these two binding sites displayed different binding affinities or maturation times for their Ndc80 interactions, we generated deletion constructs in which only one of the two sites was preserved (Fig. 2B). Both sites bound ~1 Ndc80 molecule quickly, suggesting a similar affinity, and the Ndc80 dissociation upon washout was also bi-phasic for both sites (Fig. 2C; *SI Appendix,* Fig. S5B). The lack of single-step dissociation kinetics strongly implies that maturation is an intrinsic property of each site. Indeed, with increasing incubation time, we observed the strengthening of Ndc80 binding. By 60 min, site 1 retained 0.3 ± 0.1 Ndc80 molecules whereas site 2 retained 0.8 ± 0.1 molecules (Fig. 2C,D).

To test our conclusion that the sites differ primarily in their maturation rates, we developed a detailed chemical-kinetic model for Ndc80 binding to CENP-T (*SI Appendix,* Fig. S6A, Note 3). This computational model provided an excellent fit to experimental kinetic curves when two sites were assumed to have the same binding affinity in the nascent states and ~200-fold increased affinity in the mature states (*SI Appendix,* Fig. S7A-D). In this model, a maturation rate for site 1 was 4-fold slower than for site 2 (*SI Appendix,* Table S1). Slower maturation of site 1, which is predicted to form a less extended interface with Spc24/25 (Fig. 2A; *SI Appendix,* Note 2), suggests that site maturation is linked to a conformational transition in CENP-T as it wraps around the Spc24/25 head.

To further test our conclusions, we used these kinetic constants to predict results for Ndc80 binding to different CENP-T proteins present in a soluble form. Using Fluorescence Correlation Spectroscopy (FCS), we observed the bi-phasic complex formation in highly diluted solutions of Ndc80 and CENP-T, as well as concentration dependencies predicted by the model (Fig 2E,F*; SI Appendix,* Fig. S8, Note 4). The quantitative consistency between our results using coverslip-immobilized CENP-T and soluble proteins strongly implies that site maturation is a bona-fide property of the CENP-T-Ndc80 interaction.

Clustering of CENP-T accelerates maturation of Ndc80 binding sites

In mitotic cells, interactions between soluble monomeric CENP-T and Ndc80 molecules are poor, whereas multimerized CENP-T scaffolds form high-affinity load-bearing bonds with Ndc80 proteins within the high-density molecular meshwork of the mitotic kinetochores (8, 11, 21). Thus, we investigated Ndc80 binding to multimeric CENP-T clusters. CENP-T proteins were conjugated to a dodecahedral “mi3” 60-mer, used as a core particle (28, 29) (Fig. 3A; *SI Appendix,* Fig. S9B). Based on their fluorescence intensity, the clusters contained 46.2 ± 1.2 CENP-T-GFP molecules (Fig. 3B; *SI Appendix,* Fig. S9F-H), approaching the maximal occupancy of the mi3 core. As with individual CENP-T molecules, up to 2 Ndc80 molecules rapidly and specifically associated with each clustered CENP-T molecule (Fig. 3C,D; *SI Appendix,* Fig. S10A,B, Note 1, section 2). Following Ndc80 washout, the Ndc80 dissociation was bi-phasic, but clustered CENP-T retained a substantially larger fraction of stably-bound Ndc80 molecules than monomers (Fig. 3D). After 2 min incubation with 200 nM Ndc80, each clustered CENP-T associated on average with one strongly bound and one weakly bound Ndc80 molecule. We increased soluble Ndc80 concentrations up to 1 μM, but the fraction of stably-bound molecules was unchanged, consistent with achievement of steady-states for both molecules (Fig. 3E; *SI Appendix,* Fig. S10C). However, in deviation from the classical single-step interaction mechanisms, increasing the incubation time led to increased fraction of strongly bound Ndc80 molecules (Fig. 3F). Furthermore, changes in the Ndc80 retention by CENP-T clusters occurred at a rate that exceeded the maturation rate of CENP-T monomers. Thus, Ndc80 binding sites mature into high-affinity states faster within the high density CENP-T clusters.

To reveal the molecular underpinning of this maturation behavior, we determined the interaction between Ndc80 and individual binding sites within CENP-T clusters. Using clusters of CENP-T^{site1} and CENP-T^{site2} proteins, we found that site 2 alone retained a similar number of Ndc80 molecules as the clustered CENP-T protein with both sites (Fig. 3G,H; *SI Appendix,* Note 1, section 3). Site 1 also matured in a clustered form faster than as a monomer, but its maturation rate increased only 2.5-fold, compared with the 38-fold acceleration of site 2, which stably retained the maximally possible one Ndc80 molecule after just 2 min binding (Fig. 3 H,I; *SI Appendix,* Fig. S11A). Thus, although both Ndc80 binding sites are sensitive to the molecular environment, site 2 is largely responsible for enhanced Ndc80 binding *in vitro*. The enhanced sensitivity of site 2 within CENP-T clusters is consistent with our AlphaFold2-based finding that it forms a more extended interface with the Spc24/25 head of the Ndc80 protein than site 1 (*SI Appendix,* Note 2). This result is particularly intriguing given that CENP-T in some vertebrate organisms, including the well-studied chicken protein, has only one site for Ndc80 binding that appears to be more similar to human site 2 than site 1 (22).

Ndc80 binding sites on CENP-T exhibit differential clustering-dependent regulation in mitotic cells

The differential sensitivity of two Ndc80 binding sites to clustering provides a rich framework for the regulatory control of kinetochore assembly *in vivo*. Thus, we tested whether Ndc80 recruitment by these sites in cells follows the same pattern as in our experiments *in vitro*. Since it is challenging to distinguish the recruitment of Ndc80 via different sites and pathways at intact kinetochores, we took advantage of our sensitized outer kinetochore assembly assay, which allowed us to gauge the impact of molecular density (21). We fused a 242 amino acid N-terminal CENP-T to a single-chain monoclonal antibody (scFv), and co-expressed it in HeLa cells with a tdTomato-tagged scaffold that contained multiple repeats of the antibody's cognate epitope, GCN4pep (30) (Fig. 4A). By varying the number of GCN4pep repeats, we formed multimers consisting of 1-12 CENP-T molecules with different sequences. Expression of unclustered CENP-T^{WT} resulted in a low fraction of mitotic cells, similar to uninduced cells (Fig. 4B). However, increasing multivalency by increasing the number of GCN4pep repeats on the scaffold in cells expressing the same level of CENP-T^{WT} protein led to a pronounced mitotic arrest, indicating assembly of cell-cycle disrupting kinetochore particles (*SI Appendix,* Fig. S12; (21)). Next, we generated CENP-T constructs with only one active Ndc80 site using an alanine substitution to inactivate the other site. CENP-T multimers with the deactivating T11A substitution in site 1 (CENP-T^{T11A}) mirrored the clustering-dependency of CENP-T^{WT} (Fig. 4B; *SI Appendix,* Fig. S12). Conversely, the CENP-T mutant with the deactivating T85A substitution in site 2 (CENP-T^{T85A}) exhibited reduced potency, aligning with our expectations from *in vitro* experiments using mutants with deleted sites or lacking specific phosphomimetic substitutions (*SI Appendix,* Fig. S13, Note 5).

The mitosis-specific toxicity of CENP-T multimers may result from a competition between CENP-T particles and endogenous kinetochores for Ndc80 binding (21). To investigate this possibility directly, we quantified kinetochore-localized Ndc80 levels in these cells. All mutants failed to displace Ndc80 from kinetochores at lower CENP-T copy numbers (Fig. 4C,D). However, as the size of cytoplasmic CENP-T^{WT} multimers increased, kinetochores gradually lost Ndc80 down to 20%, concomitant with the formation of Ndc80-containing particle aggregates. CENP-T^{T11A}, containing only active site 2, exhibited an Ndc80-stripping effect similarly to CENP-T^{WT}, although at a slightly larger clustering size. In contrast, CENP-T^{T85A}, containing active site 1, showed less activity, resulting only in a 60% reduction of kinetochore-bound Ndc80 in the presence of CENP-T 12-mers. These results demonstrate that site 2 displays stronger activation in response to CENP-T oligomer size. Thus, different maturation rates observed *in vitro* for the two CENP-T binding sites correlates with differential sensitivity of Ndc80 recruitment to these sites in mitotic cells. We conclude that the molecular density-dependent acceleration of the slowly maturing binding sites biases Ndc80 recruitment to the assembling kinetochore, while avoiding formation of cytoplasmic complexes owing to their low affinity.

Discussion

The mechanisms that control hierarchical protein assembly remain a prominent focus in contemporary research due to its strong potential for applications in medicine and nanoengineering (31, 32). It is also of a fundamental importance for understanding biophysical principles that enable assembly of higher-order structures within the complex cellular environment. Here, we investigated the kinetic mechanisms of a critical assembly reaction at mitotic kinetochores, which are vital for the accurate passing on of genetic information. In fully assembled kinetochores, the outer kinetochore components are linked via load-bearing connections to a meshwork of inner kinetochore scaffolding proteins, raising questions about how kinetochore components form high-affinity bonds within the higher-order structure, while avoiding direct pairwise interactions in the cytosol. Our work reveals a density-dependent kinetic barrier for the maturation of individual binding sites (Fig. 4E). The binding between Ndc80 and CENP-T molecules is fast and density-independent, proceeding in two steps: the initially weak bonds mature into strong ones, increasing their affinity by 2 orders of magnitude. However, the maturation of individual Ndc80-CENP-T complexes in a soluble form is too slow to give rise to stable assemblies on a physiological time scale, which creates a rate-limiting barrier for stable complex formation. This maturation rate is accelerated significantly in a dense CENP-T cluster, ensuring that high-affinity bonding takes place specifically at the assembling structures. This environment-specific bond maturation is an intrinsic property of interacting partner molecules, as it does not require any additional chaperones or regulatory enzymes. We propose that this density-dependent acceleration of the otherwise slow two-step binding reaction directs preferential Ndc80 recruitment to assembling kinetochores.

To explain the molecular underpinning of site maturation and its density dependence, we speculate that the high-affinity binding interface capable of withstanding strong forces is formed when the binding site within the unstructured N-terminus of CENP-T wraps fully around the Spc24/25 head to form a tri-partite "S-wrap" configuration (Fig. 2A; *SI Appendix,* Note 2). Spontaneous formation of this topologically-complex interface may be challenging, in tune with the established multi-step behavior of binding reactions involving disordered proteins (25, 26). Dense molecular environment may accelerate "S-wrap" formation by steric or multivalent interactions with neighboring molecules. A similar activating influence of a densely crowded environment has been previously proposed for phase-separating proteins (33, 34), suggesting that activation of CENP-T site by dense molecular environment may rely on similar mechanisms.

The enhanced sensitivity of site 2 within CENP-T clusters is consistent with the predicted formation of a more extended interface with the Spc24/25 head than site 1. Maturation of the two Ndc80 binding sites in CENP-T and their different rates provide the opportunity for a novel regulatory mechanism to control kinetochore-microtubule interactions. CENP-T sites maturation may be modulated by various physiological factors, including yet unknown posttranslational modifications, other kinetochore proteins, or forces that stretch Ndc80-CENP-T linkages (Fig. 4F). Previous studies of microtubule attachment and error correction at kinetochores emphasized the controlled binding affinity between Ndc80 complex and microtubules (35), whereas the Ndc80-CENP-T linkage was assumed to persist stably throughout mitosis. Our findings suggest that kinetochore-microtubule attachments could also be stabilized by regulation of the Ndc80 affinity to CENP-T owing to binding site maturation. The tunable recruitment of Ndc80 molecules to the two spatially-separated binding sites on CENP-T may also assist in the formation of the proper nanoscale architecture of the microtubule-end coupling machinery, which enables efficient motion and force transduction (36, 37).

The type of density-dependent affinity enhancement identified here for Ndc80-CENP-T binding can facilitate biogenesis of structures that rely on strong site-specific bonds (38), as well as modulate the activity of more transient oligomers and clusters, such as involved in signaling activity (39, 40), and chromatin-associated hubs (41). Thus, emergent behaviors involving slow binding-site maturation and density-induced acceleration could assist biomolecular self-organization and may facilitate engineering of self-assembling nanoparticles for medical and technological applications.

Materials and Methods

Cloning

All CENP-T constructs were generated using a custom pET28-based vector. The vector design for all constructs involved an N-terminal CENP-T fragment (1-242 aa) followed by a 3xSGGGG repeat, eGFP, another 3xSGGGG repeat followed by a myc-tag, Spy-Tag, and a 6xHis tag (pET28-eGFP-SpyTag vector). The CENP-T^{6D} construct was generated by inserting a synthesized cDNA (Genewiz) of CENP-T containing six phosphomimetic mutations (T11D, T27D, S47D, T85D, T195D, S201D) into the pET28-eGFP-SpyTag vector through subcloning. CENP-T^{WT} construct was created by subcloning DNA fragment encoding CENP-T (1-242 aa) from pKG174 (1) into the pET28-eGFP-SpyTag vector. Constructs CENP-T^{T11D}, CENP-T^{T85D} and CENP-T^{2D} were generated using QuikChange II Site-Directed Mutagenesis Kit (Agilent, 200523) by the introduction of point mutations T85D and T11D to CENP-T^{WT}. CENP-T^{site1} and CENP-T^{site2} constructs were produced using Q5® Site-Directed Mutagenesis Kit (NEB, E0554S) by deletion of base pairs encoding amino acids from 76 to 106 and 2 to 30 from CENP-T^{2D} correspondingly. CENP-T^{TR} construct was also produced analogously by deletion of base pairs encoding amino acids from 1 to 106 from CENP-T^{2D}. To optimize expression and purification of CENP-T^{site1}, CENP-T^{site2} and CENP-T^{TR} GST-tag with TEV protease cleavage site was subcloned to 5' of CENP-T fragment. The CENP-$T^{2D,short}$ construct was created by subcloning a synthesized cDNA fragment (Genewiz) of CENP-T (1-106 aa) with two phosphomimetic mutations (T11D and T85D) into the pET28-eGFP-SpyTag vector.

The construct for mi3-based core particles was derived from the SpyCatcher-mi3-6xHis plasmid (Addgene plasmid #112255). A single modification was made by introducing a subcloned FLAG-tag encoding DNA at the 3' end of mi3 and the 5' end of 6xHis. The SNAP-SpyCatcher plasmid was derived from a plasmid encoding SNAP-GBP-6xHis, as described by (2) DNA fragment encoding GBP was substituted with the DNA encoding SpyCatcher obtained from the 6xHis-SpyCatcher-mi3 plasmid. The 6xHis tag was positioned at the C-terminal end of SpyCatcher in the resulting construct.

SunTag scaffolds were obtained from pcDNA4TO-mito-mCherry-24xGCN4_v1 (Addgene plasmid #60913). Scaffolds were cloned into lentiviral plasmids generated from Lenti-Cas9-2A-Blast (Addgene plasmid #73310). CENP-T^{WT} was obtained from pKG174 (1). CENP-T^{T11A}, CENP-T^{T85A}, and the scFv-sfGFP tag were synthesized by Twist Bioscience. scFv-sfGFP-CENP-T constructs were cloned into a repair template for the AAVS1 "safe harbor" locus (pNM280).

Cell line generation

Cell lines were generated in a HeLa cell background using Cheeseman lab HeLa cells. Doxycycline-inducible scFv-sfGFP-CENP-T cell lines were generated by homology-directed insertion into the AAVS1 "safe-harbor" locus. Donor plasmid containing selection marker, the tetracycline-responsive promoter, the transgene, and reverse tetracycline-controlled transactivator flanked by AAVS1 homology arms (3) was transfected using Lipofectamine 2000 (Thermo Fisher Scientific) with a pX330-based plasmid (4) expressing both spCas9 and a guide RNA specific for the AAVS1 locus (pNM220; gRNA sequence – 5'-GGGGCCACTAGGGACAGGAT). Cells were selected with 0.5 µg ml^{-1} puromycin (Life Technologies). Clonal lines were obtained by fluorescence activated cell-sorting single cells into 96 well plates.

SunTag scaffolds were introduced by lentiviral transduction. Lentivirus was generated by using Xtremegene-9 (Roche) to co-transfect the scaffold-containing pLenti plasmid, VSV-G envelope plasmid, and Delta-VPR or psPAX2 (Addgene plasmid #12260) packaging plasmids into HEK-293T cells (5). Other lentivirus cell lines were selected with 2 µg ml^{-1} blasticidin (Life Technologies). Cell lines containing SunTag scaffolds were generated from clonal parental lines expressing the desired sfGFP-scFv-CENP-T construct at comparable levels.

Cell Culture

HeLa cells were cultured in Dulbecco's modified Eagle medium (DMEM) supplemented with 10% fetal bovine serum (FBS), 100 U ml^{-1} penicillin and streptomycin, and 2 mM L-glutamine at 37 °C with 5% CO_2. TetOn cell lines were cultured in FBS certified as tetracycline-free. TetOn constructs were induced with 1 µg ml^{-1} doxycycline for 24 hours. To arrest cells in mitosis, cells were treated with 10 µM S-trityl-L-cysteine (STLC) for 16 hours. HeLa cells were regularly monitored for mycoplasma contamination.

Immunofluorescence

Cells were seeded on poly-L-lysine (Sigma-Aldrich) coated coverslips. Cells were pre-extracted with 0.25% PBS-Tx (PBS with 0.25% Triton X-100), then fixed in 4% formaldehyde in PBS. Coverslips were washed with 0.1% PBS-Tx (PBS with 0.1% Triton X-100) and blocked in AbdiI (20 mM Tris-HCl, 150 mM NaCl, 0.1% Triton X-100, 3% bovine serum albumin (BSA), 0.1% NaN_3, pH 7.5). Primary antibodies were diluted in AbdiI. Centromeres were detected with anti-centromere antibodies (1:100 dilution; Antibodies, Inc, 15-234-0001), and Ndc80 complex was detected with anti-Bonsai antibodies (1:4,800 dilution; (6). Cy3- and Cy5-conjugated (or Alexa 647-conjugated) secondary antibodies (Jackson ImmunoResearch Laboratories) were diluted 1:300 in 0.1% PBS-Tx. DNA was stained with 1 μg ml Hoechst-33342 (Sigma-Aldrich) in 0.1% PBS-Tx. Coverslips were mounted with PPDM (0.5% *p*-phenylenediamine, 20 mM Tris-HCl, pH 8.8, 90% glycerol). Images were acquired with a DeltaVision Ultra High-Resolution microscope (Imsol). All images are maximal intensity projections in z. image manipulation was performed in Fiji (7).

Integrated fluorescence intensity of mitotic centromeres was measured with a custom CellProfiler 4.0 pipeline (8) (adapted from (9)). The median intensity of a 5-pixel region surrounding each centromere was multiplied by the area of the centromere to determine background intensity and subtracted from the integrated fluorescence of each centromere. Regions with high GFP signal were masked to avoid measuring kinetochore proteins bound to GFP-tagged constructs. Values for each cell were calculated from the mean of the Ndc80 complex signals of kinetochores in that cell. Before calculating the mean for a cell, the Ndc80 signal of each kinetochore in the cell was normalized to anti-centromere antibody signal from that kinetochore. Overall means and statistics were calculated from pooled data from multiple experiments. To make results comparable between experiments, the mean for each cell was normalized to the mean of all cells in the 1xGCN4pep sample in the same experiment. All image quantifications were performed on raw pixel values.

DNA content analysis

Cells were incubated in 1 μg ml^{-1} doxycycline for 24 hours. 5 mM EDTA, 20 μg ml^{-1} Hoechst-33342 (Sigma-Aldrich), and 10 μM Verapimil (Tocris; Spirochrome) were added directly to media for 30 minutes to 1 hour to detach cells from the plate and stain them. Cells were collected and filtered through 35 μm nylon mesh (Falcon). Hoechst, GFP, and tdTomato signals were measured on an LSRFortessa (BD Biosciences) flow cytometer. Results were analyzed with FlowJo software. The fraction of cells in each cell cycle phase was determined in FlowJo with a Watson (Pragmatic) model using the Cell Cycle tool. The DNA content of at least 5,000 cells was analyzed for each condition for each experiment.

Protein expression and purification

CENP-T constructs (CENP-T^{6D}, CENP-T^{WT}, CENP-T^{2D}, CENP-T^{T11A}, CENP-TT^{T85A}, and CENP-T^{2D,short}) were expressed in ArcticExpress (DE3) *Escherichia coli* (Agilent Technologies, 230192*)*. Expression was induced using 0.5 mM isopropyl β-D-1-thiogalactopyranoside (IPTG) and grown for 22 h at 10 °C. Cells were lysed by sonication in ice-cold Buffer A (50 mM Tris-HCl pH 8.0, 300 mM NaCl, 5 mM β-mercaptoethanol) supplemented with 0.15 mg ml^{-1} lysozyme (Sigma-Aldrich, L6876), cOmplete EDTA-free protease inhibitors cocktail (Roche, 11873580001) and 1 mM phenylmethylsulfonyl fluoride (Sigma-Aldrich, P7626). Cell debris was cleared by ultracentrifugation in a Beckman 50.2Ti rotor at 50,000 *g* for 30 min, 4 °C. Cleared supernatant was applied to an equilibrated 5 ml HisTrap HP column (Cytiva, 17524801) on a fast protein liquid chromatography (FPLC) system AKTA Pure (GE Healthcare) at 4 °C. The column was washed with ten volumes of Buffer A, five volumes of the same buffer supplemented with 25 mM imidazole, and five volumes of buffer with 50 mM imidazole. The protein was eluted with ten column volumes of Buffer A containing the gradient of imidazole in the range 50-500 mM. Protein elution was monitored by absorbance at 280 nM and fractions containing CENP-T proteins were selected after sodium dodecyl sulfate-polyacrylamide gel electrophoresis (SDS-PAGE) analysis. Fractions containing CENP-T were combined, concentrated with 10 kDa Amicon Ultra Centrifugal Filter Units (EMD Millipore, UFC901008), and centrifuged to remove aggregates at 30,000 *g* for 15 min, 4 °C. The soluble fraction was applied to HiLoad Superdex 200 pg column (Cytiva, 28-9893-35) equilibrated with Buffer A on FPLC system AKTA Pure. Buffer A was applied at a flow rate 0.5 ml min^{-1}, all at 4 °C. Based on the SDS-PAGE analysis, the fractions containing CENP-T proteins are in the 70-80 ml range (*SI Appendix*, Fig. S1A). Finally, purified proteins were supplemented with 20% glycerol, aliquoted, flash-frozen in liquid nitrogen, and stored at -80 °C.

CENP-T^{site1}, CENP-T^{site2} and CENP-T^{TR} constructs were expressed and purified following same procedure with several modifications. First, the lysis buffer (Buffer A) was supplemented with cOmplete protease inhibitors cocktail (Roche, 11697498001) and 0.5 mM EDTA. Second, instead of using a HisTrap HP column, the clear lysate was loaded onto a Glutathione Sepharose 4B column (Cytiva, 17-0756-01) that was pre-equilibrated with Buffer A containing 0.5 mM EDTA. The column was washed with 20 column volumes of Buffer A, and the proteins were eluted by cleavage from the column using 50 µg ml^{-1} homemade TEV protease (expressed and purified from a plasmid pTrc99 7xH TEV received as a gift from Dr. Lampson, University of Pennsylvania) in Buffer A with 0.5 mM EDTA overnight at 4 °C. The fractions containing the target proteins were then concentrated and loaded onto a HiLoad Superdex 200 pg column, following the same procedure as described above.

SNAP-SpyCatcher and SNAP-GBP proteins were expressed in BL21(DE3) *Escherichia coli* (NEB, C2527H). Expression was induced using 0.1 mM IPTG and grown for 18 h at 16 °C. Cells were lysed using a microfluidic chamber in ice-cold Buffer B (50 mM NaH_2PO_4 pH 8.0, 300 mM NaCl, 1 mM DTT, 0.1% Tween20 (Sigma-Aldrich, P1379) supplemented with 1 mg ml^{-1} lysozyme, 1 mM 4-(2-aminoethyl)benzenesulfonyl fluoride hydrochloride (AEBSF, Santa Cruz Biotechnology, sc-202041A) and 10 mM imidazole. After centrifugation at 50,000 g for 30 min, 4 °C supernatant was filtered and incubated with Ni-nitrilotriacetic acid (Ni-NTA) agarose (Qiagen, 30210) for 1 h at 4 °C. Bound protein was washed with Buffer B supplemented 20 mM imidazole and 1 mM AEBSF. The protein was eluted with Buffer B supplemented with 250 mM imidazole. To reduce the concentration of imidazole in the eluate, the buffer was changed to Buffer B without imidazole using Ultra Centrifugal Filter Units (EMD Millipore, UFC901008). Protein fractions were supplemented with 20% glycerol, aliquoted, snap-frozen in liquid nitrogen, and stored at -80 °C.

SNAP-GBP was labeled with SNAP-Surface Alexa Fluor 647 (NEB, S9136S). The conjugation reaction was carried out in Buffer B without Tween20 using 12 µM Alexa Fluor 647 dye and 4 µM SNAP-GBP, with a 3-fold excess of dye over the protein. The reaction was allowed to proceed for 3 hours at room temperature. To separate unbound dye from labeled protein reaction mixture was loaded to PD-10 column (Cytiva, 17085101) column and eluted by Buffer B without Twin20. Finally, SNAP-GBP labeled with Alexa Fluor 647 was supplemented with 20% glycerol, aliquoted, flash-frozen in liquid nitrogen, and stored at -80 °C. In the paper for simplicity we call this protein "GBP-Alexa Fluor647".

Human Bonsai Ndc80 complex containing the N-terminal fragment of Hec1 (1-286 aa) fused to a fragment of the Spc25 (118-224 aa) with C-terminal GFP or untagged and the Nuf2 protein (1-169 aa) fused to a fragment of Spc24 (122-197 aa) was expressed in *Escherichia coli* and purified, as in (10) (*SI Appendix*, Fig. S1A). Human Ndc80 ΔSpc24/25 complex containing N-terminal fragments of Hec1 (1-506 aa) and Nuf2 (1-348 aa) with GFP-tag on the C-terminus of Nuf2 was expressed and purified, as in (6).

The protocol for purification of mi3-based core particles (6xHis-SpyCatcher-mi3) was based on (11). Mi3-based core particles were expressed in BL21(DE3) *Escherichia coli*. Expression was induced using 0.5 mM IPTG overnight at 22 °C. Cells were lysed and sonicated in ice-cold Buffer C (50 mM Tris-HCl pH 8.5, 500 mM NaCl) supplemented with 0.15 mg ml^{-1} lysozyme, cOmplete EDTA-free protease inhibitors cocktail and 1 mM phenylmethylsulfonyl fluoride. Cell debris were cleared by ultracentrifugation in a Beckman 50.2Ti rotor at 50,000 *g* for 30 min, 4 °C. Cleared supernatant was applied to equilibrated 5 ml HisTrap HP column on a FPLC system AKTA Pure at 4 °C. The column was washed with ten volumes of Buffer C, five volumes of the same buffer supplemented with 25 mM imidazole, and five volumes of buffer with 50 mM imidazole. The protein was eluted with ten column volumes of Buffer C containing the gradient of imidazole in range of 50-500 mM. Protein in elution was monitored by absorbance at 280 nM and fractions containing 6xHis-SpyCatcher-mi3 were selected after SDS-PAGE-analysis. Fractions containing SpyCatcher-mi3 were combined, concentrated to 5 ml with 100 kDa Amicon Ultra Centrifugal Filter Units and centrifuged to remove aggregates at 30,000 *g* for 15 min, 4 °C. The soluble fraction was applied to HiPrep 16/60 Sephacryl S-400 column equilibrated with Buffer C on FPLC system AKTA Pure.

Buffer C was applied at flow-rate 0.5 ml min^{-1}, all at 4 °C. Based on the SDS-PAGE-analysis, the fractions containing 6xHis-SpyCatcher-mi3 particles are in the 60-75 ml range. Mi3-based core particles were supplemented with 20% glycerol, aliquoted, flash-frozen in liquid nitrogen and stored at -80 °C.

Assembly of CENP-T clusters in solution

For electron microscopy (EM) experiments (Fig. 3A; *SI Appendix*, Fig. S9B), CENP-T clusters were assembled in a test tube and subsequently purified using gel-filtration chromatography. 80 nM of SpyCatcher-mi3 core particles were conjugated to 10 µM of Spy-tagged CENP-T^{2D,short}. The conjugation reaction was carried out in buffer D (50 mM Tris-HCl pH 8.0, 150 mM NaCl) for 3 hours at room temperature. Separation of the conjugated clusters from unconjugated CENP-T was performed by loading the reaction mixture onto a HiPrep 16/60 Sephacryl S-400 column. The column was equilibrated and washed with buffer D at a flow rate of 0.5 ml min^{-1}. The CENP-T^{2D,short} clusters were eluted in the range of 60-75 ml, supplemented with 20% glycerol, aliquoted, flash-frozen in liquid nitrogen, and stored at -80 °C.

TIRF microscopy assay to study the interactions between monomeric CENP-T and soluble Ndc80

Flow chamber preparation and imaging. Prior to each experiment, frozen protein aliquots of SNAP-SpyCatcher, Ndc80, and CENP-T were thawed on ice and clarified by ultracentrifugation at 156,000 *g* for 15 min at 4 °C. Flow chambers were prepared as described in (12) using silanized coverslips and reusable glass slides with tubing (13). To perfuse solutions into the flow chamber, a syringe pump (New Era Pump Systems, NE-4000) was used to draw the liquid at a speed of 150 µL min^{-1}, unless otherwise indicated. The specimen on the microscope stage was maintained at 32 °C. The coverslip of the assembled and sealed flow chamber was functionalized by incubation with 100 nM of SNAP-SpyCatcher in PBS buffer (10.1 mM Na_2HPO_4, 1.8 mM KH_2PO_4 pH 7.2, 140 mM NaCl 2.7 mM KCl) supplemented with 2 mM DTT for 10 min. Next, the chamber surface was blocked with 1% Pluronic F127 (Sigma-Aldrich, CP2443). Then, 1-3 nM of CENP-T-GFP-Spy-tag in PBS buffer supplemented with 2 mM DTT, 4 mg ml^{-1} BSA (Sigma-Aldrich, A7638) and 0.5 mg ml^{-1} casein (Sigma-Aldrich, C5890) were introduced for 5 min to achieve the desired density of CENP-T molecules on the coverslip (Fig. 1C). Chambers were then incubated with Imaging Buffer: Mg-BRB80 (80 mM K-PIPES pH 6.9, 1 mM EGTA, 4 mM $MgCl_2$) supplemented with 10 mM DTT, 4 mg ml^{-1} BSA and 0.5 mg ml^{-1} casein, 0.1 mg ml^{-1} glucose oxidase (Sigma-Aldrich, G2133), 20 µg ml^{-1} catalase (Sigma-Aldrich, C40) and 6 mg ml^{-1} glucose (Sigma-Aldrich, G8270).

All fluorescent imaging was performed using a Nikon Eclipse Ti microscope equipped with a 1.49xNA TIRF 100x Oil objective. Excitation for visualizing GFP- and Alexa Fluor 647-tagged proteins in TIRF modes was provided by coherent CUBE 488-nm and 640-nm 50 mW diode lasers (Coherent). Images were captured using an Andor iXon3 EMCCD camera. The concentration of GFP-tagged proteins was determined by measuring GFP intensity through fluorescence microscopy, as described in (12).

Before the addition of Ndc80, a set of images of immobilized GFP-tagged CENP-T molecules in several imaging fields was captured to determine their initial coordinates and intensities. Subsequently, 200 µl of 200 nM GFP-tagged Ndc80 in Imaging Buffer were introduced using a syringe pump at a speed of 900 µl min^{-1}. The same fluorophore was used on CENP-T and GFP molecules to simplify intensity quantification and avoid errors caused by uneven or varying illumination. The interaction time between Ndc80 and CENP-T varied in experiments, ranging from 2 to 60 minutes. At specific time points, a second image of one of the initial fields was captured to observe the brightness of the dots. At indicated times, soluble Ndc80 was washed out by perfusing 200 µl of Imaging Buffer at a speed of 900 µl min^{-1}. Then, the pump speed was reduced to 5 µl min^{-1} and the flow was maintained to remove any remaining Ndc80 molecules that detached from CENP-T clusters over time. During the unbinding phase, images of a different set of initially captured fields were collected at the desired time points.

Data analysis. The images of CENP-T molecules were analyzed using the Fiji software (7). First, the pair of images before and after Ndc80 addition was manually corrected for a stage drift. Then, the 30-40 GFP-tagged CENP-T molecules were manually selected on the initial CENP-T image. If a CENP-T molecule detached during the experiment, it was not considered for further analysis. The fluorescence intensity was measured in the area surrounding the CENP-T molecule (3-pixel radius) on both images. The brightness of the same-sized area located near the selected molecule was subtracted to minimize variability in background intensity. To confirm that immobilized CENP-T molecules are monomeric, the distribution of their initial fluorescence intensities was normalized to the fluorescence of one GFP molecule (Fig. 3B; *SI Appendix*, Fig. S1E-J). For that, the fluorescence intensities of individual GFP and Alexa Fluor 647 fluorophores were determined using photobleaching curves, as described in (14) (*SI Appendix*, Fig. S1C,D). The number of bound Ndc80 molecules was calculated as the difference between the intensity after Ndc80 binding and the initial CENP-T-GFP intensity, divided by the initial intensity. For each time point corresponding to the pair of experimental images, the median Ndc80 binding was determined. Next, the median Ndc80 binding was plotted against time, and specific portions of the curve representing Ndc80 binding and unbinding were fitted using one-component exponents (Fig. 1D,E). For the unbinding exponent, the initial point was set to be similar to the plateau of the binding exponent. The total binding level was determined as the plateau of the exponent fitting the binding curve, while the stable binding level was determined as the plateau of the exponent fitting the unbinding curve. The k_{off} rate was obtained as the exponent parameter of the unbinding curve fitting. The transient binding was determined as a difference between total and stable binding.

To evaluate the binding of GBP-Alexa Fluor647 to GFP-tagged CENP-T the analogues procedure was done with the following modification. First, the number of CENP-T molecules for one GFP dot was quantified by dividing the dot’s fluorescence intensity by the intensity of one GFP molecule (*SI Appendix*, Fig. S1C). Then, the number of GBP-Alexa Fluor647 molecules was quantified by dividing the dot’s fluorescence in the second fluorescent channel by the intensity of one Alexa Fluor647 molecule (*SI Appendix*, Fig. S1D). Finally, the number of GBP-Alexa Fluor647 molecules was divided by the number of CENP-T molecules to get the efficiency of binding.

Estimation of photobleaching effect. Since photobleaching of GFP molecules on CENP-T can potentially affect the accurate quantification of Ndc80 binding to CENP-T, imaging conditions were selected to minimize the probability of photobleaching. The illumination time was minimized to 0.3 s, and each experimental field was captured only twice: initially before Ndc80 addition and at a specific time after Ndc80 addition. To estimate probability of photobleaching of GFP molecules over this illumination time (0.6 s), the rate of photobleaching was measured using GFP-tagged CENP-T^{6D} molecules immobilized on the coverslip. Imaging field with GFP-tagged CENP-T^{6D} molecules was continuously illuminated using the same illumination settings as those used in experiments with CENP-T monomers. The number of GFP dots per imaging field at each time point was counted and normalized to the number of dots in the first imaging frame. Data from N = 3 independent experiments were combined and the resultant curve was fitted to an exponential decay function to determine the exponent coefficient (*SI Appendix*, Fig. S2B). The probability of photobleaching was then calculated as the illumination time 0.6 s multiplied by the exponent coefficient, resulting in 6%. This probability is within the range of experimental error from multiple experimental repeats, so it is not expected to significantly affect the results.

TIRF microscopy assay to study the interactions between clustered CENP-T and soluble Ndc80

Preparation of CENP-T clusters in a flow chamber and imaging. The flow chamber was constructed as in experiments with CENP-T monomers. After the chamber was blocked with Pluronic F127, mi3-based core clusters (100 nM) were allowed to adsorb on the coverslip for 10 min. Next, 200 nM of CENP-T in PBS buffer supplemented with 2 mM DTT, 4 mg ml^{-1} BSA and 0.5 mg ml^{-1} casein were introduced for 20 min at room temperature. This binding time is enough for conjugation of ~40

CENP-T molecules per one mi3-based core particles (Fig. 3B; *SI Appendix*, Fig. S9F-H). Chamber with assembled CENP-T clusters was rinsed with Imaging Buffer.

At all stages of experiment the images of clusters were acquired in TIRF mode with a 488 nm 100 mW diode laser (Coherent, Santa Clara, CA, USA) at 1% power with an exposure time of 30 ms. Several images of GFP-tagged CENP-T clusters were collected for subsequent quantifications of their initial fluorescence intensity, corresponding to the quantity of CENP-T molecules per cluster. The clusters were then bleached with laser at 100% power for 30 s. Several images of CENP-T clusters were collected after bleaching to evaluate the efficiency of bleaching and remaining GFP intensity of clusters. The subsequent stages of the experiments, involving the binding and unbinding of Ndc80, were conducted in a similar manner to the experiments performed with monomeric CENP-T. The only difference was that images of the clusters within the same imaging field were continuously captured at a rate of 12 images per minute, allowing for the monitoring of changes in GFP-intensity over time. Unlike single molecule settings, the laser power was significantly reduced for cluster imaging, and there was no requirement to capture different fields for different time points. Some experiments with CENP-T clusters were carried out in the presence of a continuous flow (30 µl min^{-1}) of Imaging Buffer with Ndc80 protein, but in others the flow was used only to introduce Ndc80 into the chamber. This variation did not affect final binding results, so the data for stable Ndc80 binding were combined.

Data analysis. To evaluate level of Ndc80 binding, image sequences with CENP-T clusters were analyzed similarly to monomers with several modifications. First, for stage drift correction of the image stack the "Manual drift correction" plugin in Fiji software was used (7). Second, the area in which fluorescence intensity was measured was increased up to 8-pixel radius to fit CENP-T clusters. Finally, the initial fluorescence intensity of clusters was not subtracted from intensity of clusters after Ndc80 addition due to bleaching of GFP molecules on CENP-T clusters. Typically, approximately 30 clusters were analyzed for each independent experiment.

Correction for photobleaching. To estimate and correct effect of GFP-photobleaching the photobleaching curve for on GFP-tagged CENP-T clusters was measured. For that GFP-tagged CENP-T^{6D} clusters immobilized on the coverslip as described above were continuously illuminated and imaged with microscope settings identical to those used for experiments with CENP-T clusters. Than integral intensity of clusters were calculated for each time point as described above and normalized on intensity on initial time frame. Dependency of clusters's intensity vs. illumination time was fitted with exponential decay (*SI Appendix*, Fig. S9D). Resulting exponent was used as photobleaching curve.

To take into account photobleaching of GFP-molecules over time, experimental data corresponding to unbinding of Ndc80 from CENP-T clusters were normalized on photobleaching curve. While, soluble GFP-tagged Ndc80 molecules can exchange on CENP-T clusters during biding phase, data from this stage of experiment were not corrected on bleaching. Total illumination time during binding phase of experiment was < 3.6 s, that corresponds to bleaching of < 5% of GFP-molecules.

Quantification of CENP-T's cluster size. The size of GFP-tagged CENP-T clusters was calculated based on their fluorescence intensity. First, the intensity of individual GFP-molecule was captured at following settings for Andor iXon3 camera: 10 MHz readout speed, gain 5.0x, EM gain 999, 30 msec exposure time; and 50% power of 488 nm 100 mW diode laser (Coherent, Santa Clara, CA, USA), as described in (14). Next, GFP-tagged CENP-T clusters immobilized on the coverslip were captured on the same camera settings, except laser power, which was reduced from 50% to 1% to avoid camera saturation due to high fluorescence intensity of clusters. Then, the images of clusters were corrected on the laser intensity profile, which was obtained, as described in (14), by averaging images with high density of CENP-T clusters on the coverslip. Finally, number of GFP-tagged CENP-T molecules per cluster was calculated as ratio of fluorescence intensity of individual clusters divided on intensity of single GFP molecule and multiplied on coefficient 31.2 ± 1.3 to take into account difference in laser power settings.

To determine a coefficient of conversion for fluorescence intensity between 1 % and 50 % laser power settings in TIRF mode the calibration curve was plotted (*SI Appendix*, Fig. S9E). To achieve a wide range of pixel values and measure the calibration curve, specific camera settings were used, including a 1 MHz camera readout speed, gain of 5.0x, no EM gain, and a 300-millisecond exposure time. GFP-tagged CENP-$T^{2D,short}$ clusters were attached to the coverslip of the microscopic chamber in Imaging Buffer, and different sets of imaging fields (n = 5) were captured at each laser power settings. The coefficient of transition between 1% and 50% laser power was calculated as the ratio of the corresponding data points.

FCS assay

FCS measurements were performed on a multi-parameter time-resolved confocal microscopy and spectroscopy instrument (MicroTime-200, PicoQuant, Germany). GFP-tagged CENP-T proteins were excited with 484 nm pulsed diode laser (LDH-D-TA-484, PicoQuant) operating at 20 MHz, through an excitation dichroic filter ZT440-445/484-491/594 rpc-UF3 (Chroma Technology) and an Olympus UPLanSApo 60x/1.2-W water objective lens. The laser power was maintained at ~15 μW and it was focused 20 μm above the coverslip interface for measurement. After passing through a 50 μm pinhole, the fluorescence signals from the sample were split into two channels by a polarized beam splitter (U-MBF3-Olympus). The signals further passed through bandpass filters ET535/70 (Chroma Technology) and projected onto two single-photon avalanche photodiode detectors (SPAD: SPCM-AQRH-14-TR). Nunc Lab-Tek chambers (ThermoFisher, 155411) with borosilicate cover slip bottoms were used at 19-21 °C. The chambers were passivated by treatment with 50% PEG-8000 solution, incubated at room temperature for 3-4 hours, followed by 3-4 washes with the Mg-BRB80 buffer. Atto-488 dye was used as a standard sample to calibrate the confocal detection volume of the 484 nm laser beam.

Ndc80 binding experiments were carried out by rapid mixture of 1 nM GFP-tagged CENP-T with 0-1000 nM of unlabeled Ndc80 Bonsai in Mg-BRB80 buffer supplemented with 2 mM DTT and 4 mg ml^{-1} BSA and 0.5 mg ml^{-1} casein.

The analysis of time-trace curves was performed using the SymPhoTime software provided by PicoQuant. To ensure accurate results, the time-trace signals were filtered with an 80-count threshold to eliminate aggregates, followed by background correction. Cross-correlation curves were generated using signals from two detectors and fitted with a triplet model (*SI Appendix*, Fig. S8A-D) (15).

Negative Staining Electron Microscopy

Mi3-based clusters, either empty or preassembled with CENP-$T^{2D,short}$, were applied to freshly glow-discharged carbon-coated 200 mesh copper grids (Electron Microscopy Sciences, CF200-CU-50) and incubated for 1 minute. Excess liquid was blotted off using filter paper. The grids were then washed three times and stained with 2% uranyl acetate for 30 seconds. After staining, the excess stain was blotted off, and the grids were air-dried. Imaging of the grids was performed using a JEM 1011 transmission electron microscope (JEOL) operated at 100 kV, coupled with an ORIUS 832.10W CCD camera (Gatan). The size of clusters was estimated with Fiji software.

Structural analysis of Ndc80-CENP-T complexes using AlphaFold2

The structures of Ndc80 and CENP-T individually, as well as in complex, were obtained utilizing AlphaFold2.2.4. (16). Each prediction was done with following options: model type “alphafold2_multimer_v3”, 5 models were recycled until the model tolerance was less than 0.5, all five models underwent amber relaxation (17). The model with the first rank was selected for subsequent analysis.

As AlphaFold2 inputs sequences provided in PDB database were used: 3VZA (18) for chicken proteins Spc24(134-195 aa)/Spc25(134-232 aa) in complex with CENP-T(63-93 aa; T72D, S88D); 2VE7 (19) for human Spc24(122-197 aa)/Spc25(118-224 aa); sequences of human CENP-T fragments 1-30 aa and 76-106 aa with phosphomimetic substitutions T11D and T85D were used identical to constructs used in this work (NCBI: KAI2579221.1).

The analysis and alignment of the predicted structures was conducted using the PyMOL Molecular Graphics System, Version 2.5 (Schrödinger, LLC). To quantify structural similarities, the template modeling (TM) score was calculated using the Python tmtools package version 0.0.3 (20, 21).

Mathematical modeling

Theoretical approaches and our model are described in *SI Appendix*. Briefly, interactions between Ndc80 and CENP-T were analyzed by determining numerical solutions of a system of differential equations for different proteins and initial conditions. The model predicted fraction of Ndc80-CENP-T complexes as a function of time and Ndc80 concertation. MATLAB version R2020b with a MATLAB ODE solver *ode45* were used.

Acknowledgments: We are grateful to Drs. Yale E. Goldman and Him Shweta (University of Pennsylvania) for their guidance, training, and insightful suggestions during FCS experiments. We thank Drs. Tatyana M. Svitkina and Anil Chougule (University of Pennsylvania) for their guidance and assistance with electron microscopy imaging. We thank Dr. Haitao Li and Tatyana Kogan for assistance with cloning and purifications of CENP-T proteins, Vladimir M. Demidov for assistance with data analysis, Veronika Balakshina and Polina Soloveva for technical assistance. Dr. Jennifer G. Deluca and Jeanne E. Mick (Colorado State University) kindly provided the plasmid with untagged Ndc80 Bonsai and advised on the purification of Ndc80 constructs; Dr. Michael A. Lampson (University of Pennsylvania) kindly provided a plasmid with TEV protease. We also thank Drs. Yale E. Goldman, E. Michael Ostap, Ben E. Black, Michael A. Lampson, Mathew C. Good, their lab members, members of the Philly Chromo Club and members of the Grishchuk lab for thoughtful and insightful discussions.

Funding: This work was supported by a grant to ELG from NIH/NIGMS (R35-GM141747), grants to IMC from the NIH/NIGMS (R35GM126930), including diversity supplement funding for GBS, and the Gordon and Betty Moore Foundation, and grants to both IMC and ELG from the American Cancer Society Theory Lab Collaborative Grant (TLC-20-117-01-TLC) and NSF (2029868); grants RNF 22-15-00164 to FIA.

Author Contributions: EVT designed and performed all *in vitro* experiments. GBS and IMC designed and performed experiments using HeLa cells. AM and EVT constructed and purified recombinant proteins, performed molecular structure and sequence analysis. FIA and ASM developed and carried out mathematical modeling. ELG and EVT designed the research project, analyzed the data, and wrote the paper with input from IMC and other co-authors.

Competing Interest Statement: Authors declare that they have no competing interests.

Data sharing plans: Images and data that support the findings of this study are available in the main text and the supplementary materials. The Source data encompasses all data points and statistical analyses used to generate the graphs presented in the main text and the Supplement. Detailed protocols and custom programs for image analyses are deposited on the Grishchuk laboratory website as detailed in the supplementary Data Source file. Raw fluorescence intensity and FCS data are available from the corresponding author upon request.

References

1. M. G. Mateu, Assembly, stability and dynamics of virus capsids. *Archives of Biochemistry and Biophysics* **531**, 65-79 (2013).
2. A. Musacchio, A. Desai, A Molecular View of Kinetochore Assembly and Function. *Biology* **6** (2017).
3. J. R. Wisniewski, M. Y. Hein, J. Cox, M. Mann, A "proteomic ruler" for protein copy number and concentration estimation without spike-in standards. *Mol Cell Proteomics* **13**, 3497-3506 (2014).
4. D. N. Itzhak, S. Tyanova, J. Cox, G. H. Borner, Global, quantitative and dynamic mapping of protein subcellular localization. *Elife* **5** (2016).
5. A. Suzuki, B. L. Badger, E. D. Salmon, A quantitative description of Ndc80 complex linkage to human kinetochores. *Nature communications* **6**, 8161 (2015).
6. I. M. Cheeseman, The kinetochore. *Cold Spring Harbor perspectives in biology* **6**, a015826 (2014).
7. J. R. McIntosh *et al.*, Conserved and divergent features of kinetochores and spindle microtubule ends from five species. *Journal of Cell Biology* **200**, 459-474 (2013).
8. A. Suzuki *et al.*, Spindle microtubules generate tension-dependent changes in the distribution of inner kinetochore proteins. *J Cell Biol* **193**, 125-140 (2011).
9. K. E. Gascoigne, I. M. Cheeseman, CDK-dependent phosphorylation and nuclear exclusion coordinately control kinetochore assembly state. *J Cell Biol* **201**, 23-32 (2013).
10. F. Rago, K. E. Gascoigne, I. M. Cheeseman, Distinct organization and regulation of the outer kinetochore KMN network downstream of CENP-C and CENP-T. *Curr Biol* **25**, 671-677 (2015).
11. M. Hara, M. Ariyoshi, E. I. Okumura, T. Hori, T. Fukagawa, Multiple phosphorylations control recruitment of the KMN network onto kinetochores. *Nature cell biology* **20**, 1434 (2018).
12. S. Kim, H. Yu, Multiple assembly mechanisms anchor the KMN spindle checkpoint platform at human mitotic kinetochores. *J Cell Biol* **208**, 181-196 (2015).
13. Y. Yang *et al.*, Phosphorylation of HsMis13 by Aurora B kinase is essential for assembly of functional kinetochore. *The Journal of biological chemistry* **283**, 26726-26736 (2008).
14. M. K. Bonner *et al.*, Enrichment of Aurora B kinase at the inner kinetochore controls outer kinetochore assembly. *The Journal of Cell Biology* **218**, 3237-3257 (2019).
15. J. Haase, M. K. Bonner, H. Halas, A. E. Kelly, Distinct Roles of the Chromosomal Passenger Complex in the Detection of and Response to Errors in Kinetochore-Microtubule Attachment. *Dev Cell* **42**, 640-654 e645 (2017).
16. B. Akiyoshi, C. R. Nelson, S. Biggins, The aurora B kinase promotes inner and outer kinetochore interactions in budding yeast. *Genetics* **194**, 785-789 (2013).
17. A. Petrovic *et al.*, Structure of the MIS12 Complex and Molecular Basis of Its Interaction with CENP-C at Human Kinetochores. *Cell* **167**, 1028-1040 e1015 (2016).
18. E. V. Tarasovetc *et al.*, Permitted and restricted steps of human kinetochore assembly in mitotic cell extracts. *Mol Biol Cell* **32**, 1241-1255 (2021).
19. K. Killinger *et al.*, Auto-inhibition of Mif2/CENP-C ensures centromere-dependent kinetochore assembly in budding yeast. *EMBO J* **39**, e102938 (2020).
20. E. M. Kudalkar *et al.*, Regulation of outer kinetochore Ndc80 complex-based microtubule attachments by the central kinetochore Mis12/MIND complex. *Proc Natl Acad Sci U S A* **112**, E5583-5589 (2015).
21. G. B. Sissoko, E. V. Tarasovetc, O. Marescal, E. L. Grishchuk, I. M. Cheeseman, Higher-order protein assembly controls kinetochore formation. *Nature cell biology* 10.1038/s41556-023-01313-7 (2024).
22. T. Nishino *et al.*, CENP-T provides a structural platform for outer kinetochore assembly. *EMBO J* **32**, 424-436 (2013).
23. P. J. Huis In 't Veld *et al.*, Molecular basis of outer kinetochore assembly on CENP-T. *Elife* **5** (2016).

24. K. E. Gascoigne *et al.*, Induced ectopic kinetochore assembly bypasses the requirement for CENP-A nucleosomes. *Cell* **145**, 410-422 (2011).
25. L. Mollica *et al.*, Binding Mechanisms of Intrinsically Disordered Proteins: Theory, Simulation, and Experiment. *Front Mol Biosci* **3**, 52 (2016).
26. J. Dogan, S. Gianni, P. Jemth, The binding mechanisms of intrinsically disordered proteins. *Phys Chem Chem Phys* **16**, 6323-6331 (2014).
27. C. Ciferri *et al.*, Implications for kinetochore-microtubule attachment from the structure of an engineered Ndc80 complex. *Cell* **133**, 427-439 (2008).
28. Y. Hsia *et al.*, Design of a hyperstable 60-subunit protein dodecahedron. [corrected]. *Nature* **535**, 136-139 (2016).
29. T. U. J. Bruun, A. C. Andersson, S. J. Draper, M. Howarth, Engineering a Rugged Nanoscaffold To Enhance Plug-and-Display Vaccination. *ACS Nano* **12**, 8855-8866 (2018).
30. M. E. Tanenbaum, L. A. Gilbert, L. S. Qi, J. S. Weissman, R. D. Vale, A protein-tagging system for signal amplification in gene expression and fluorescence imaging. *Cell* **159**, 635-646 (2014).
31. S. Boyoglu-Barnum *et al.*, Quadrivalent influenza nanoparticle vaccines induce broad protection. *Nature* **592**, 623-628 (2021).
32. L. Shao *et al.*, Hierarchical Materials from High Information Content Macromolecular Building Blocks: Construction, Dynamic Interventions, and Prediction. *Chemical Reviews* **122**, 17397-17478 (2022).
33. H. Wu, M. Fuxreiter, The Structure and Dynamics of Higher-Order Assemblies: Amyloids, Signalosomes, and Granules. *Cell* **165**, 1055-1066 (2016).
34. P. Bhat, D. Honson, M. Guttman, Nuclear compartmentalization as a mechanism of quantitative control of gene expression. *Nat Rev Mol Cell Biol* **22**, 653-670 (2021).
35. M. A. Lampson, E. L. Grishchuk, Mechanisms to Avoid and Correct Erroneous Kinetochore-Microtubule Attachments. *Biology* **6** (2017).
36. E. L. Grishchuk, Biophysics of Microtubule End Coupling at the Kinetochore. *Progress in molecular and subcellular biology* **56**, 397-428 (2017).
37. A. A. Kukreja, S. Kavuri, A. P. Joglekar, Microtubule Attachment and Centromeric Tension Shape the Protein Architecture of the Human Kinetochore. *Curr Biol* **30**, 4869-4881.e4865 (2020).
38. A. Musacchio, On the role of phase separation in the biogenesis of membraneless compartments. *The EMBO Journal* **41**, e109952 (2022).
39. J. Liu *et al.*, Biased signaling due to oligomerization of the G protein-coupled platelet-activating factor receptor. *Nature communications* **13**, 6365 (2022).
40. R. Deliz-Aguirre *et al.*, MyD88 oligomer size functions as a physical threshold to trigger IL1R Myddosome signaling. *Journal of Cell Biology* **220** (2021).
41. A. Mora, X. Huang, S. Jauhari, Q. Jiang, X. Li, Chromatin Hubs: A biological and computational outlook. *Comput Struct Biotechnol J* **20**, 3796-3813 (2022).

Figures and Tables

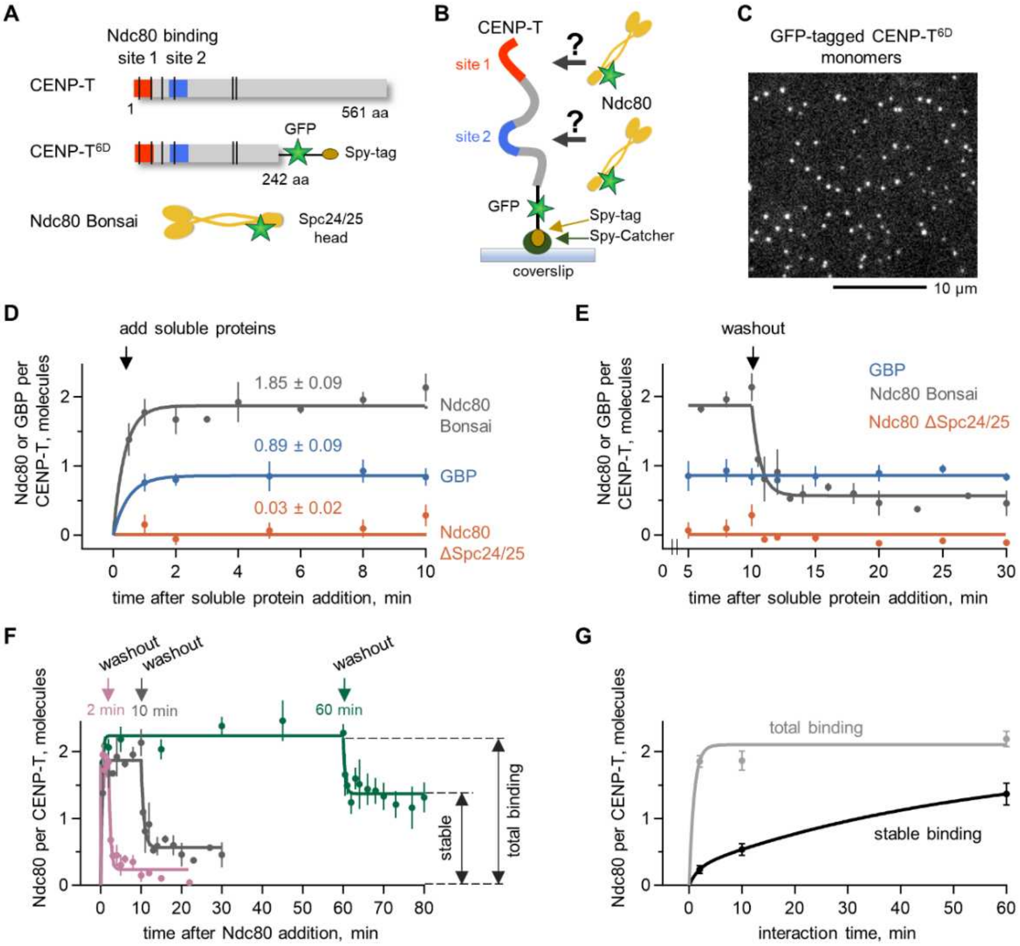

Figure 1. Ndc80 association with monomeric CENP-T and complex stability.

(A) Diagram of human CENP-T protein with phosphorylation sites. CENP-T^{6D} contains N-terminal 242 aa, six aspartate substitutions (T11D, T27D, S47D, T85D, T195D, S201D), the C-terminal GFP for visualization, and the Spy-tag for immobilization. **(B)** CENP-T^{6D}-GFP-Spy-tag molecules were immobilized via coverslip-adhered Spy-Catcher protein, and incubated with GFP-tagged Ndc80 Bonsai, which is a shortened version of Ndc80 protein with wild-type Spc24/25 domain. **(C)** Example imaging field with immobilized molecules. **(D)** Graph shows binding of different Ndc80-GFP constructs to monomeric CENP-T^{6D}. Binding is represented as the background-corrected differential between the GFP fluorescence intensity at a given time and the initial intensity at time 0, divided by the initial intensity of individual fluorescent dots. The quantification for GBP-Alexa Fluor647 is described in *SI Appendix,* Materials and Methods. Lines are exponential fittings, numbers are the steady-state binding levels with SEM. For this and other graphs in this figure, concertation of soluble proteins is 200 nM. Each data point represents N independent experiments with mean ± SEM; N is 3-8 per the data set. For detailed statistical information for this and other graphs, refer to the Source data file. **(E)** Graph shows dissociation of indicated proteins from immobilized CENP-T^{6D} monomers after removal of soluble proteins. Complexes formed between GFP on CENP-T^{6D} and the GFP nanobody (GBP) exhibited stable association with 1:1 stoichiometry. **(F)** Ndc80 binding to CENP-T^{6D} monomers and dissociation kinetics at indicated washout times. **(G)** Time-dependent changes in the total (in the presence of soluble Ndc80) and stable (after Ndc80 washout) binding of Ndc80 to CENP-T^{6D} monomers.

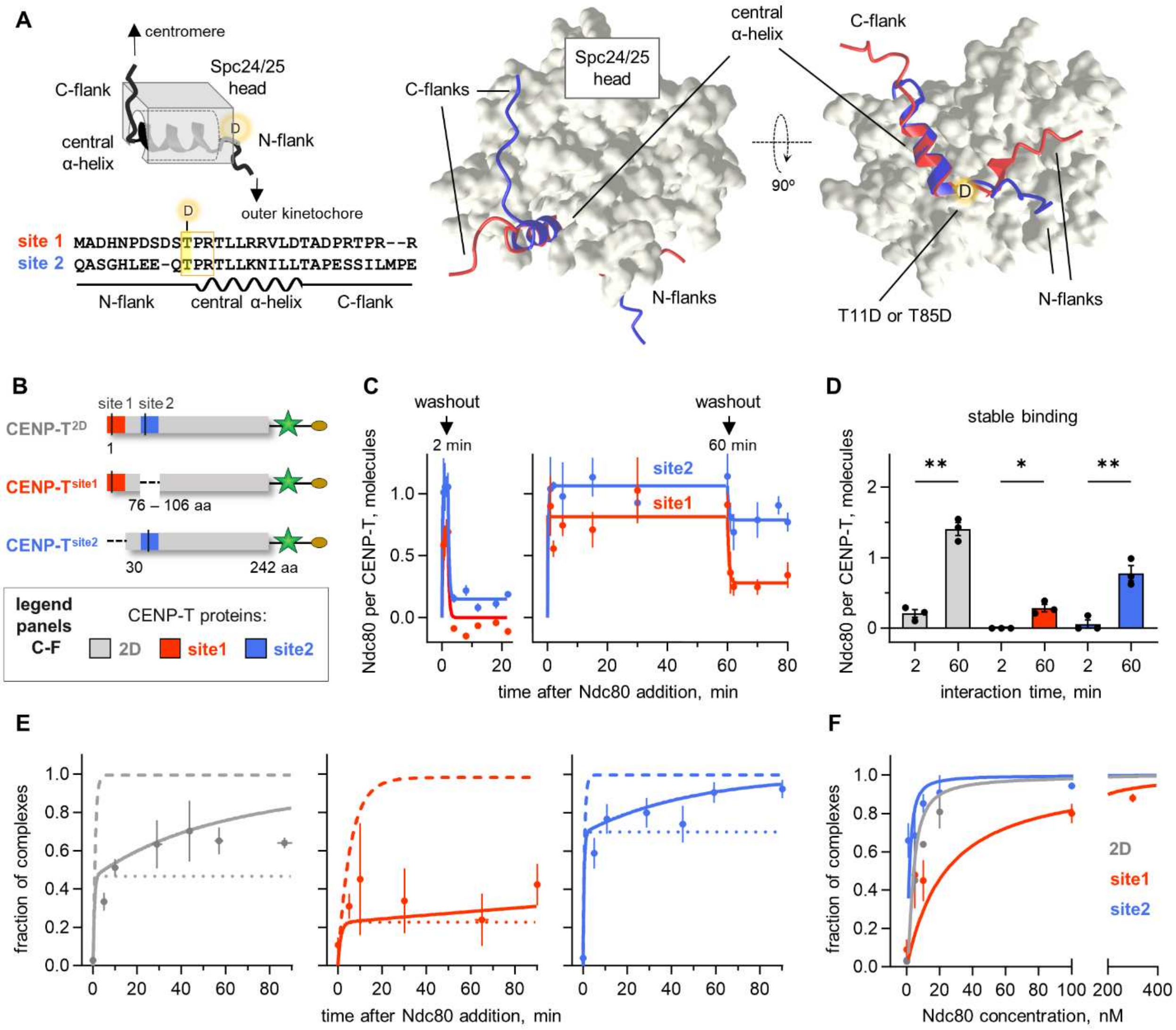

Figure 2. Behavior of individual Ndc80 binding sites in CENP-T monomers.

(A) Left: A simplified schematic of the 30 aa peptide of CENP-T (thereafter called "site") forming an S-wrap around the Spc24/25 head based on 3vzA structure for chicken proteins (22). Below: sequence alignment and predictions for human CENP-T sites; see *SI Appendix,* Note 2 for details. Right: AlphaFold2-based predictions for human CENP-T sites binding to Spc24/25 head. The central α-helix of both sites is inserted into a conserved Spc24/25 groove, but configurations of the flanking regions are different. **(B)** Diagram of the CENP-T^{2D} (2D), CENP-T^{site1} (site1), and CENP-T^{site2} (site2) constructs. **(C)** Number of Ndc80s bound per indicated coverslip-immobilized CENP-T monomer. Soluble Ndc80 (200 nM) was added at time 0 and removed as indicated. Each point is mean ± SEM, N = 3; lines are exponential fittings. **(D)** Stable binding of Ndc80 to indicated coverslip-immobilized CENP-T constructs. Each point represents mean ± SEM determined in independent experiment with n > 20 molecules per each time point, here and below n stands for number of molecules/clusters in an independent experiment. For all graphs the unpaired t-test with Welch's was used: not significant (ns) corresponds to $p > 0.05$, * to $p < 0.05$, ** to $p < 0.01$, *** to $p < 0.001$, and **** to $p < 0.0001$. **(E)** Kinetics of complex formation for 10 nM Ndc80 and 1 nM CENP-T protein studied with FCS. Here and in panel (F) points are experimental data (mean ± SEM, N =

2-5), lines are predictions of different models: solid line – model with site maturation, broken lines – conventional binding with different dissociation constants, see *SI Appendix,* Note 3. For CENP-T^{2D}, fraction of complexes with two Ndc80 molecules is plotted. **(F)** Fraction of indicated Ndc80-CENP-T complexes as a function of soluble Ndc80 concentration; CENP-T is 1 nM. Lines show predictions of the model with maturation.

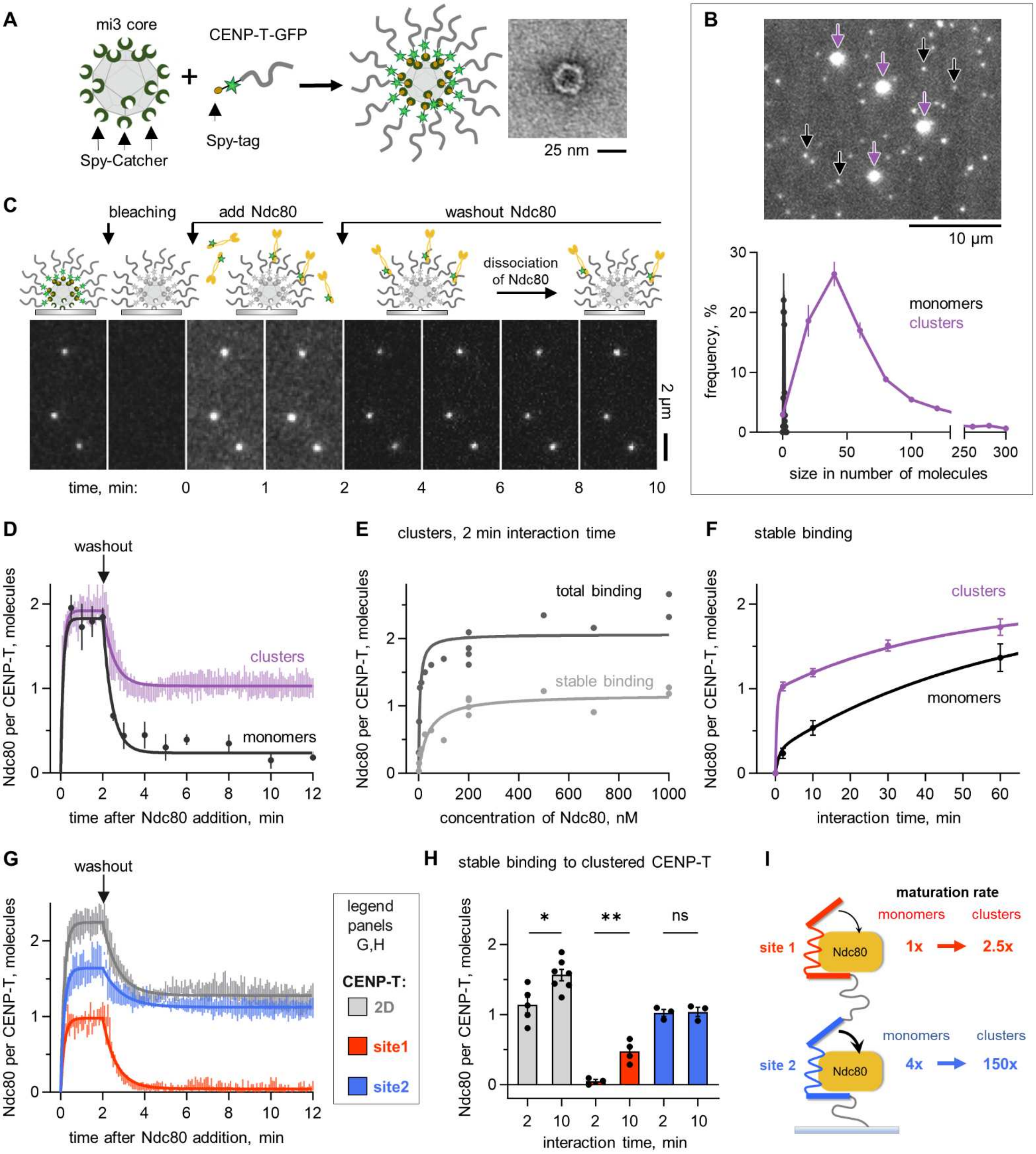

Figure 3. Ndc80 association with CENP-T clusters and binding stability.

(A) CENP-T multimerization strategy and an electron microscopy image of the assembled cluster. **(B)** Representative GFP-fluorescence image of the coverslip-immobilized GFP-tagged CENP-T^{6D} monomers (black arrows) and their mi3-based clusters (purple arrows), and the corresponding size distribution histograms. For graphs in panels (B), (D), (F), (G), each point represents mean ± SEM, N = 3-24. **(C)** Schematics of the experiment and representative images of GFP-tagged CENP-T^{6D} clusters; unless indicated otherwise, Ndc80-GFP was 200 nM. **(D)** Number of Ndc80 molecules per one CENP-T^{6D} molecule within the cluster vs. monomers (same as in Fig. 1F). Data in (D), (F) and (G) are fitted with exponential functions. **(E)** Number of Ndc80 molecules per one CENP-T^{6D} molecule within the cluster as a function of Ndc80 concentration for 2-min washouts. Lines are hyperbolic fits; in panels (E) and (H), each point represents an independent experiment with n > 12; bars show mean ± SEM. **(F)** Kinetics of stable complex formation between Ndc80 and CENP-T^{6D} molecules in clustered vs. monomeric (same as in Fig. 1G) form. **(G)** Fast binding and bi-phasic dissociation of Ndc80 and indicated CENP-T clusters. **(H)** Stable binding of Ndc80 to indicated CENP-T clusters after different interaction time. **(I)** The diagram summarizing quantitative findings for maturation of sites in monomeric vs. clustered CENP-T^{6D}. Ndc80 (Spc24/25 head) is shown binding to two interfaces of each CENP-T site, symbolizing weak binding by the nascent CENP-T. Maturation is depicted with the curved black arrows that bring the third interface in contact with Ndc80, thereby increasing the binding strength. The numbers are normalized maturation rates relative to the slowest transition seen in site1 in CENP-T monomers ($2 \cdot 10^{-4}$ s^{-1}), as determined using our mathematical model.

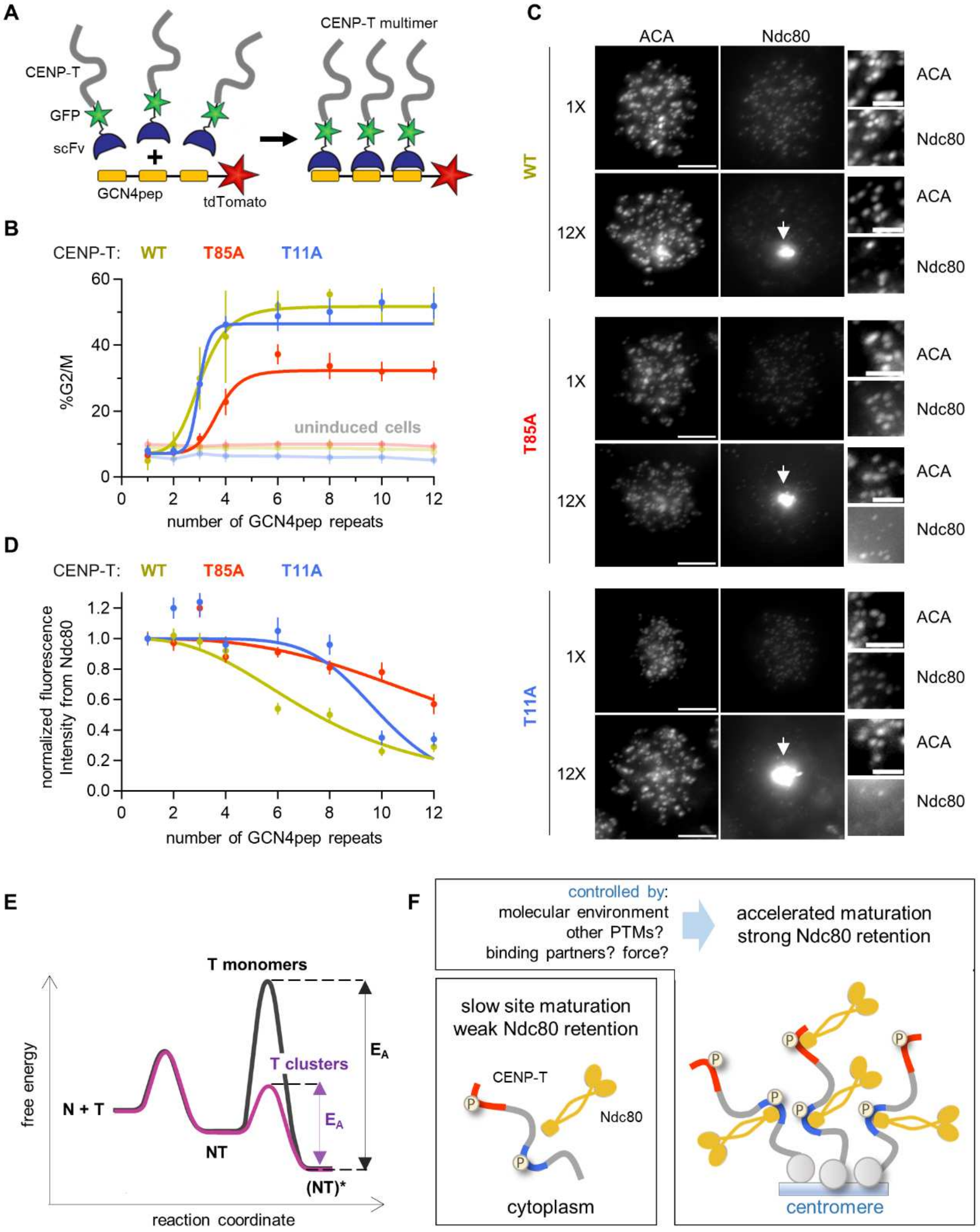

Figure 4. Distinct clustering-dependent regulation of Ndc80 binding sites on CENP-T in mitotic cells.

(A) Diagram illustrating the sensitized outer kinetochore assembly assay utilizing Sun-Tag tunable oligomerization, see text for details. **(B)** Percent of G2/M cells for cells expressing indicated CENP-T constructs, which were oligomerized using SunTag scaffolds with different numbers of GCN4pep. Data for uninduced cells are shown in faded colors. Each point represents the mean ± SEM from N = 2-4 independent experiments, lines are fits with a sigmoidal function. Data in panel (B) and (D) for CENP-T^{WT} construct are from (21), and are provided here for a direct comparison. **(C)** Representative images of mitotic cells showing localization of kinetochores and CENP-T oligomers with the indicated number of repeats (white arrows). The centromeres (ACA) and Ndc80 are visualized with immunofluorescence Images with different CENP-T constructs have different image adjustments, and the insets are adjusted differently from the full-size images for improved visibility. Scale bar: 5 µm. **(D)** Same experiments as in panel (B) but showing Ndc80 kinetochore level; 23-46 total cells for each condition pooled from N = 3 for CENP-T^{WT} and N = 2 for CENP-T^{T11A} and CENP-T^{T85A}. **(E)** The free energy difference (not to scale) between the unbound and complexed Ndc80 (N) and CENP-T (T) proteins plotted against the reaction coordinate. NT – binding state with weak Ndc80 retention. Activation energy barrier (E_A) for a strong-affinity state (NT)* is controlled by the molecular density of CENP-T. **(F)** Simplified schematics of the established and proposed mechanisms to control direct Ndc80 recruitment by CENP-T scaffold. For simplicity, shortened molecular variants are depicted and other kinetochore proteins are omitted.

SI Appendix. Mathematical modeling of Ndc80 interaction with CENP-T

Maturation of CENP-T binding sites is manifested by the presence of two fractions with disparate dissociation constants (*SI Appendix*, Fig. S2D). The initial weak association with the nascent sites appears to transform into the strong retention at the “mature” sites as a result of a stochastic site transition rather than the slow evolution of sites with a continuum of binding affinities. We formalized this site-maturation hypothesis with the following reaction scheme for one binding site:

$$N + T \underset{k_{off}}{\overset{k_{on}}{\rightleftarrows}} (NT) \overset{k_{mat}}{\rightarrow} (NT)^* \underset{k_{off}^*}{\rightarrow} N + T \qquad \text{(S1)}$$

where N corresponds to Ndc80, T to Ndc80 binding site on CENP-T, (NT) and $(NT)^*$ to nascent and mature Ndc80-CENP-T complexes correspondingly. Rate constants k_{on} and k_{off} describe Ndc80 association and dissociation with the nascent CENP-T site, whereas k_{off}^* corresponds to dissociation of the mature complex and k_{mat} describes the transition from nascent to mature site.

Because the sites mature autonomously (*SI Appendix*, Note 1, section 3), this scheme is applicable to any of the two Ndc80 binding sites on CENP-T, but for the molecule with both sites the reaction transition scheme is more complex (*SI Appendix*, Fig. S6A). For the unbiased quantitative examination of this reaction scheme, we constructed a chemical kinetics model, which includes both sites and their respective transitions.

General overview of theoretical approaches

First, we constructed the model to describe interactions between soluble Ndc80 protein and CENP-T monomers immobilized on the coverslip surface. Ndc80 binding at each site was described with association and dissociation rate constants. The applicability of the mass action law for surface-immobilized molecules, and our use of probability-based modeling in conjunction with the fractions of interacting molecules are discussed below. All kinetic constants for this model were determined (model calibration) by fitting to experimental kinetic curves generated in experiments with coverslip-immobilized CENP-T monomers.

This model for immobilized CENP-T monomers was used to describe experimental results for the coverslip-immobilized CENP-T clusters and soluble Ndc80.

The model for immobilized CENP-T was adjusted to predict reactions between Ndc80 and CENP-T in solution. All kinetic parameters for Ndc80 binding/unbinding were identical to those in the model for coverslip-immobilized CENP-T monomers.

Application of the mass action law to reactions with the surface-immobilized molecules

According to the mass action law, the rate of a chemical reaction is directly proportional to the concentrations of the reactants. This law is well-suited for systems with a large number of reacting particles in a homogeneous medium. However, this approach needs modification when studying reactions involving surface-associated molecules. To adjust the mass action equation for a surface-bound reactant A, we analyzed the likelihood of interaction between molecule A and a freely diffusing molecule B in the solution. Similar to reactions occurring in solution, we assumed that the interaction between A and B occurs when these two molecules collide and subsequently undergo a chemical reaction. Consequently, the probability of interaction between molecules A and B (denoted as p^{inter}) is determined by multiplying the probabilities of their collision p^{AB} and the subsequent chemical reaction p^{react}.

To calculate the probability of collision, we first considered a general case when molecules of reactant A are distributed on a surface area S, which is in contact with a homogeneous solution of the freely floating molecules B (*SI Appendix*, Fig. S6C). We assumed that the surface distribution of molecules A is random, and the distance between the adjacent molecules is larger than the effective interaction radius S^{eff}. The probability p^{smB} of one molecule B with diameter d_B to collide with the immobilized molecule A with diameter d_A is given by:

$$p^{smB} = \frac{S^{eff}}{S} = \frac{\frac{1}{4}\pi(d_A+d_B)^2}{S} \tag{S2}$$

The probability of collision p^{AB} between any soluble molecule B and any immobilized molecule A should be proportional to the concentration of molecules B, denoted by $[B]$. We assume that during the reaction $[B]$ is high enough to neglect changes in concentration due to complex formation with molecules A, so $[B] = [B_0]$, where $[B_0]$ is the initial concentration of molecules B. Additionally, p^{AB} should be proportional to the surface density of molecules A that have not yet formed a complex with B, denoted by $< A >$. Thus, the probability of collision p^{AB} is given by:

$$p^{AB} = p^{smB} < A > [B_0] \tag{S3}$$

$$p^{AB} = \frac{\frac{1}{4}\pi(d_A+d_B)^2}{S} < A > [B_0] \tag{S4}$$

Thus,

$$p^{inter} = p^{react} p^{AB} \sim < A > [B_0] \tag{S5}$$

Applying equation (S5) to experiments that track binding between immobilized and soluble molecules presents a challenging task. The results of such experiments cannot be interpreted in terms of concentrations, and the initial surface density of molecules A, denoted by $< A_0 >$, is often unknown. Moreover, when studying single molecules, the binding outcome is binary, indicating whether the complex has formed or not, further complicating the application of equation (S5). To address these challenges, we considered the fraction of immobilized single molecules A that have not formed a complex with molecule B, denoted by $\{A\}$. We used the normalized probability of interaction $p^{measured}$, which is independent of the initial density $< A_0 >$:

$$p^{measured} = \frac{p^{inter}}{<A_0>} \sim \frac{<A>[B_0]}{<A_0>} \sim \{A\}[B_0] \tag{S6}$$

Thus, the reaction rate v, which is proportional to $p^{measured}$, is given by

$$v = k\, p^{measured} \sim k\,\{A\}[B_0], \tag{S7}$$

where k is the corresponding kinetic constant.

Equation (S7) enables the construction of a system of differential equations that describe interactions between coverslip-immobilized CENP-T molecules and soluble Ndc80. The solutions of this system can be directly compared to experimental data.

Model for soluble Ndc80 and coverslip-immobilized CENP-T monomers

Model framework

Ndc80 protein. In the model, the concentration of soluble Ndc80 protein (in nM), denoted by $[N]$ was constant and equal to its initial concentration $[N_0]$, which was selected according to experimental conditions. Here and below the square brackets stand for the concentration of the corresponding soluble reactant.

CENP-T protein with nascent Ndc80-binding sites. Modeling was carried out for CENP-T molecules with two Ndc80 binding sites, denoted by two numbers as subscripts of the letter *T*. CENP-T has four possible Ndc80-binding configurations T_{ij} (i refers to site 1, j refers to site 2): $T_{00}, T_{10}, T_{01}, T_{11}$. Subscript is 0 when the corresponding site is free from Ndc80, subscript is 1 when Ndc80 is bound to the corresponding site.

Maturation. Additionally, the Ndc80 binding sites on CENP-T can "mature". Maturation was modeled as a probabilistic event that reduced the rate of Ndc80 dissociation from the CENP-T site with bound Ndc80 molecule. Thus, maturation in the model is the first-order irreversible transition with a corresponding kinetic rate constant called the "maturation" constant (k_{mat}). Configurations of CENP-T molecules with mature sites are indicated with an asterisk: T_{i^*j}, T_{ij^*}, $T_{i^*j^*}$ $(i,j = \overline{0,1})$. We also assume that the site remains mature upon Ndc80 unbinding. For simplicity, in CENP-T configurations with both mature sites occupied by Ndc80, we assumed that binding is very stable and neglects Ndc80 dissociation. Because the dissociation rate from the mature site is very low (see below), this assumption did not affect significantly model results.

Thus, there are 13 possible configurations of CENP-T in the model. The total number of CENP-T molecules in all configurations remains constant during calculations and equals the initial number of molecules denoted by $[T_0]$. The ratio of the number of CENP-T molecules in configuration T_{ij} to $[T_0]$ is represented with $\{T_{ij}\}$, where curly braces stand for the fraction of CENP-T in the corresponding configuration.

Reaction scheme and equations for Ndc80 and CENP-T interactions

All reactions are summarized in *SI Appendix*, Fig. S6A. Transitions between different nascent sites are depicted with large black arrows, showing the corresponding molecular constants. Transitions from nascent to mature forms are depicted with thick red and blue arrows, showing the corresponding maturation constants.

Ndc80 recruitment was modeled as a series of reversible chemical reactions between N and 13 different configurations of CENP-T. For simplicity, during one step, each T can bind only one molecule N, where symbol T with no subscripts refers to CENP-T molecule in any possible configuration.

Binding of N is described as a second-order chemical reaction characterized by association rate constants k_{1on} and k_{2on} depending on the binding site.

Dissociation of N from any of T site was described as a first-order reaction characterized by a dissociation constant: k_{1off} or k_{2off} correspond to Ndc80 dissociation from the nascent (not matured) sites, whereas k^*_{1off} or k^*_{2off} correspond to the mature sites.

Maturation of each site is independent and with maturation constant k_{1mat} for site 1 and k_{2mat} for site 2. This assumption was based on our experimental results showing that the sites mature autonomously (*SI Appendix*, Fig. S5C, S10G).

The following differential equations correspond to this reaction scheme, where t is time.

$$\frac{d\{T_{00}\}}{dt} = -k_{2on}[N]\{T_{00}\} + k_{2off}\{T_{01}\} - k_{1on}[N]\{T_{00}\} + k_{1off}\{T_{10}\} \qquad \text{(S8)}$$

$$\frac{d\{T_{01}\}}{dt} = k_{2on}[N]\{T_{00}\} - k_{2off}\{T_{01}\} - k_{1on}[N]\{T_{01}\} + k_{1off}\{T_{11}\} - k_{2mat}\{T_{01}\} \qquad \text{(S9)}$$

$$\frac{d\{T_{10}\}}{dt} = k_{1on}[N]\{T_{00}\} - k_{1off}\{T_{10}\} - k_{2on}[N]\{T_{10}\} + k_{2off}\{T_{11}\} - k_{1mat}\{T_{10}\} \qquad \text{(S10)}$$

$$\frac{d\{T_{11}\}}{dt} = k_{1on}[N]\{T_{01}\} - k_{1off}\{T_{11}\} + k_{2on}[N]\{T_{10}\} - k_{2off}\{T_{11}\} - k_{1mat}\{T_{11}\} - \\ - k_{2mat}\{T_{11}\} \qquad \text{(S11)}$$

$$\frac{d\{T_{0^*0}\}}{dt} = -k_{2on}[N]\{T_{0^*0}\} + k_{2off}\{T_{0^*1}\} - k_{1on}[N]\{T_{0^*0}\} + k^*_{1off}\{T_{1^*0}\} \qquad \text{(S12)}$$

$$\frac{d\,\{T_{0^*1}\}}{dt} = k_{2on}[N]\{\,T_{0^*0}\} - k_{2off}\{T_{0^*1}\} - k_{1on}[N]\,\{T_{0^*1}\} + k^*_{1off}\,\{T_{1^*1}\} \qquad \text{(S13)}$$

$$\frac{d\{T_{1^*0}\}}{dt} = k_{1on}[N]\{T_{0^*0}\} - k^*_{1off}\{T_{1^*0}\} - k_{2on}[N]\{T_{1^*0}\} + k_{2off}\{T_{1^*1}\} + k_{1mat}\{T_{10}\} \qquad \text{(S14)}$$

$$\frac{d\,\{T_{1^*1}\}}{dt} = k_{1on}[N]\,\{T_{0^*1}\} - k^*_{1off}\{T_{1^*1}\} + k_{2on}[N]\{T_{1^*0}\} - k_{2off}\,\{T_{1^*1}\} + k_{1mat}\,\{T_{11}\} - \\ - k_{2mat}\,\{T_{1^*1}\} \qquad \text{(S15)}$$

$$\frac{d\,\{T_{00^*}\}}{dt} = -k_{2on}[N]\{T_{00^*}\} + k^*_{2off}\{T_{01^*}\} - k_{1on}[N]\{T_{00^*}\} + k_{1off}\{T_{10^*}\} \qquad \text{(S16)}$$

$$\frac{d\,\{T_{01^*}\}}{dt} = k_{2on}[N]\,\{T_{00^*}\} - k^*_{2off}\{T_{01^*}\} - k_{1on}[N]\,\{T_{01^*}\} + k_{1off}\,\{T_{11^*}\} + k_{2mat}\{T_{01}\} \qquad \text{(S17)}$$

$$\frac{d\{T_{10^*}\}}{dt} = k_{1on}[N]\{T_{00^*}\} - k_{1off}\{T_{10^*}\} - k_{2on}[N]\{T_{10^*}\} + k^*_{2off}\{T_{11^*}\} \qquad \text{(S18)}$$

$$\frac{d\,\{T_{11^*}\}}{dt} = k_{1on}[N]\,\{T_{01^*}\} - k_{1off}\,\{T_{11^*}\} + k_{2on}[N]\,\{T_{10^*}\} - k^*_{2off}\,\{T_{11^*}\} - k_{1mat}\{T_{11^*}\} + \\ + k_{2mat}\,\{T_{11}\} \qquad \text{(S19)}$$

$$\frac{d\,\{T_{1^*1^*}\}}{dt} = k_{1mat}\,\{T_{11^*}\} + k_{2mat}\{T_{1^*1}\} \qquad \text{(S20)}$$

$$\frac{d[N]}{dt} = 0 \qquad \text{(S21)}$$

$$\frac{d}{dt}\,(\{T_{00}\} + \{T_{01}\} + \{T_{10}\} + \{T_{11}\} + \{T_{0^*0}\} + \{T_{0^*1}\} + \{T_{1^*0}\} + \{T_{1^*1}\} + \{T_{00^*}\} + \{T_{01^*}\} + \\ \{T_{10^*}\} + + \{T_{11^*}\} + \{T_{1^*1^*}\}) = 0 \qquad \text{(S22)}$$

The system of first-order differential equations (S8)-(S22) was used to calculate $\{T\}$ as a function of time from the start of reactions for indicated initial conditions (see below). Then, for every time point the fraction of CENP-T in each configuration was multiplied by the number of bound Ndc80 molecules for this configuration. For example: the number of bound Ndc80s to T_{00}, T_{01} and T_{11} were 0, 1 and 2 correspondingly. Changes in the sum of all fractions adjusted in this manner correspond to the kinetics of the number of Ndc80 molecules bound to one CENP-T molecule.

Description of the calculation algorithm

The concentration of Ndc80 and the fractions of CENP-T molecules in all possible configurations are calculated at each iteration of the numerical solution of a system of differential equations. To solve differential equations we used a programming and numeric computing platform MATLAB version R2020b with a versatile MATLAB ODE solver *ode45*. Ode45 is a medium order method for non-stiff differential equations that implements a Runge-Kutta method with a variable time step for efficient computation. Total calculation time was chosen to match experimental conditions.

Initial conditions and model calibration

Binding and unbinding (wash-out) stages of experiments with coverslip-immobilized CENP-T were calculated separately.

Initial conditions. The initial concentration of Ndc80 $[N_0]$ for the binding stage was chosen to match specific experimental conditions (200 nM unless otherwise specified). In the model for soluble Ndc80 and coverslip-immobilized CENP-T, the concentration of soluble Ndc80 $[N]$ was kept constant throughout all calculations for the binding stage. To model the wash-out, soluble Ndc80 concentration was set to zero.

For calculations during the binding stage, the initial fraction of CENP-T molecules in all configurations was 0, except for $\{T_{00}\}$, which was set to 1 for normalization. For the wash-out stage, the initial fractions of CENP-T molecules in different configurations were taken from the results of corresponding calculations during the binding stage.

Model calibration. Model for soluble Ndc80 and coverslip-immobilized CENP-T monomers was calibrated by obtaining a good match between model predictions and experiments with 200 nM Ndc80 Bonsai and monomeric CENP-T^{6D} (Fig. 1F). Because Ndc80 binding was very fast, we estimated that the lower limit on the association rate constant is 10^{-3} nM^{-1} s^{-1}. The Ndc80 dissociation rate for the strongly bound Ndc80 fraction (which we attribute to the mature sites) was very slow. In view of the limited observation time (20 min) it was also not possible to determine this dissociation rate accurately. Because Ndc80 binding/unbinding to both nascent sites was similarly fast, for simplicity we assumed that the corresponding rate constants were identical. We used the association rate constant $2.5 \cdot 10^{-3}$ nM^{-1} s^{-1} and the dissociation rate constant $5 \cdot 10^{-5}$ s^{-1} for each mature site on CENP-T. The same dissociation rate constants were assumed for both nascent sites, whereas the maturation rate k_{1mat} and k_{2mat} for two sites were treated as unconstrained fitting parameters. We varied the dissociation rate constants for nascent sites and the maturation rate constants for both sites to obtain a good fit to experiments with immobilized CENP-T^{6D} monomers, as described in section “Summary of modeling results”. It resulted in 10^{-2} s^{-1} dissociation rate constant for the nascent sites and the maturation rate constants $2 \cdot 10^{-4}$ s^{-1} for site 1 and $2 \cdot 10^{-4}$ s^{-1} for site 2.The model with these parameters provided good fit to experimental time-dependencies using ~200-fold decrease in dissociation rate for mature vs. nascent site and the 4-fold slower maturation rate for site 1 vs. site 2 (Table S1).

Application of the model to describe interactions between soluble Ndc80 and coverslip-immobilized CENP-T clusters

The above model for CENP-T monomers was applied directly to describe experiments with CENP-T clusters. Because model results were presented as the number of Ndc80 molecules bound to one CENP-T molecule, modeling results can be compared directly with experimental kinetic curves. If the Ndc80 interaction with clustered CENP-T occurred with the same rate constants as with the CENP-T monomers, model predictions should be the same for both molecular forms of CENP-T. However, application of the model for CENP-T monomers to kinetic data for CENP-T clusters provided a poor fit. A much better fit was obtained using adjusted maturation constants (Table S1, see section “Summary of modeling results”).

Application of the model to describe experiments with mutant CENP-T proteins

The same reaction schemes (*SI Appendix*, Fig. S6A), equations (S8)-(S22), and model parameters were to describe experiments with CENP-T^{2D}. To describe experiments with mutant CENP-T proteins lacking one of the binding sites (CENP-T^{site1} and CENP-T^{site2}), the association, dissociation, and maturation rate constants for a deleted site were set to zero, corresponding to the lack of any interactions with this site (see section “Summary of modeling results”).

Model for soluble Ndc80 and CENP-T proteins

To predict the kinetics of complex formation in solution, the same system of equations (S8)-(S22) was used with the exception of equation (S21), which was replaced with equation (S23), as described below. Because the mass action law is directly applicable to molecular interactions in solution, the variables $\{T\}$ in this case represent soluble concentration of the corresponding CENP-T configurations.

FCS method cannot be used in solutions containing high protein concentration, so our experiments were carried out with low Ndc80 and CENP-T concentrations (10n M and 1 nM, correspondingly). Thus, we could no longer assume that the concentration of soluble Ndc80 did not change during the binding reactions with CENP-T proteins. Thus, in the adjusted model, concentrations of all soluble proteins changed over time in accordance with their binding/unbinding interactions. To take this into account, equation (S21) was replaced with the following equation:

$$\frac{d[N]}{dt} = -\, k_{1on}\,[N]\,\{T_{00}\} - \; k_{2on}[N]\,\{T_{00}\} - \; k_{2on}[N]\,\{T_{10}\} - \; k_{1on}[N]\,\{T_{01}\} + \; k_{1off}\,\{T_{10}\} + \\ + k_{1off}\,\{T_{11}\} \; + \; k_{2off}\,\{T_{01}\} + \; k_{2off}\{T_{11}\} - \; k_{1on}[N]\{T_{0^*0}\} - \; k_{2on}[N]\,\{T_{0^*0}\} - \\ k_{2on}[N]\,\{T_{1^*0}\} - -\, k_{1on}[N]\,\{T_{0^*1}\} + \; k^*_{1off}\{T_{1^*0}\} + \; k^*_{1off}\,\{T_{1^*1}\} + \; k_{2off}\,\{T_{0^*1}\} + \\ k_{2off}\,\{T_{1^*1}\} - \; k_{1on}[N]\{T_{00^*}\} - -\, k_{2on}[N]\,\{T_{00^*}\} - \; k_{2on}[N]\,\{T_{10^*}\} - \; k_{1on}[N]\,\{T_{01^*}\} + \\ k_{1off}\,\{T_{10^*}\} + \; k_{1off}\,\{T_{11^*}\} + \; + k^*_{2off}\{T_{01^*}\} + \; k^*_{2off}\,\{T_{11^*}\} \qquad \text{(S23)}$$

Furthermore, only the binding phase was analyzed, in correspondence with conditions of the FCS experiments. The initial concentration of CENP-T $[T_0]$ was 1 nM, concentration of Ndc80 $[N_0]$ was 10 nM. Model results for changes in concentrations of selected CENP-T configurations were divided by the initial concentration of CENP-T molecules, so that model predictions were presented as fractions of the formed complexes, enabling direct comparison with experiments.

For CENP-T^{2D} protein, the plotted fraction corresponds to T_{11} configuration (two Ndc80 molecules are bound). For CENP-T proteins with only one site, the plotted fractions correspond to complexes with one Ndc80 molecule. To build concentration dependencies, the initial concentration of Ndc80 $[N_0]$ was varied in the range from 0 to 300 nM and the fraction on Ndc80-CENP-T complexes was determined after 70 min interaction.

To generate predictions in the absence of site maturation, same model was used but the maturation rate constants for both sites were set to 0. Three different CENP-T proteins were modeled: CENP-T^{2D}, CENP-T^{site1} and CENP-T^{site2}. The values of association rate constants remained the same as in the model with maturation for the corresponding proteins, as listed in *SI Appendix*, Table S2. The kinetics of Ndc80 binding to CENP-T in solution was then calculated using two sets of values of the dissociation rate constants for the corresponding proteins: for the nascent and mature sites.

Summary of modeling results

1. Model for soluble Ndc80 protein and immobilized CENP-T^{6D} monomers. This model was used to fit the results of experiments for 200 nM Ndc80 and CENP-T^{6D} monomers (Fig. 1G). Specifically, three experimental curves were fit, representing interactions between Ndc80 and CENP-T^{6D} for 2, 10, or 60 minutes. Theoretical curves matched well the total and stable binding (*SI Appendix*, Fig. S7A). Based on this fit, all rate constants were determined (Table S1) and fixed for subsequent application to all other experiments.

2. Application of the model for soluble Ndc80 protein and immobilized CENP-T^{6D} monomers to describe experiments with other CENP-T monomers.

CENP-T^{2D}. The model for soluble Ndc80 protein and immobilized CENP-T^{6D} monomers with parameter values listed in *SI Appendix*, Table S1 was applied to describe results of the experiments in which 200 nM Ndc80 was added to CENP-T^{2D} monomers for 2 and 60 min. Fig. S7B shows a good match between model predictions and experimental curves. Thus, Ndc80 binding to CENP-T^{2D} and CENP-T^{6D} monomers can be fitted with the same model and same kinetic constants (Table S1), suggesting that Ndc80 binding to CENP-T is not strongly affected by the phosphomimetic substitutions T27D, S47D, T195D and S201D.

CENP-T^{site1} and CENP-T^{site2}. The model for soluble Ndc80 protein and immobilized CENP-T^{6D} monomers with parameter values listed in *SI Appendix*, Table S1 was applied to describe results of the experiments in which 200 nM Ndc80 was added to CENP-T^{site1} and CENP-T^{site2} monomers for 2 and 60 min (Fig. 2C), but the match between the model and experimental results was not optimal. To improve fitting results, the association rate constant k_{1on} for site 1 in the CENP-T^{site1} protein was reduced by a factor of 8, relative to the association rate constant for the same site in CENP-T proteins with both sites present (CENP-T^{2D} and CENP-T^{6D}). The value of the association constant k_{2on} for site 2 in the CENP-T^{site2} protein was left unchanged relative to CENP-T^{2D} and CENP-T^{6D} proteins, since it provided the adequate fit. Thus, Ndc80 binding to site 1 is enhanced when site 2 is present. Furthermore, a better fit for experimental curves was obtained when the maturation rate constants k_{1mat} and k_{2mat} were reduced by ~ 2-fold (*SI Appendix*, Fig. S7C,D, Table S2), indicating the slightly slower maturation rate of individual sites in mutant proteins. This reduction, however, does not significantly affect the stable binding and maturation of individual binding sites in mutant proteins, and in our experiments binding by individual sites was approximately additive (*SI Appendix*, Note 1, section 3).

Model for soluble Ndc80 and CENP-T proteins. This model with parameter values listed in *SI Appendix*, Tables S1 and S2 for CENP-T monomers was applied to describe results of the FCS experiments in which 1 nM CENP-T (CENP-T^{2D}, CENP-T^{site1} or CENP-T^{site2}) was incubated with 10 nM Ndc80 for 90 min (Fig. 2E points). The fraction of complexes was calculated for 0-90 time range using a 1 s time step and plotted (Fig. 2E, solid lines). The maturation-dependent binding kinetics in solution is predicted to have the initial phase with a fast increase in complex formation, corresponding to transient interactions with the nascent sites. It is followed by a slower phase, which arises owing to improved Ndc80 retention (*SI Appendix*, Fig. S7E). As alternative models, we calculated predictions for the maturation-free binding with two dissociation rates k_{off} and k^*_{off}, corresponding to weak and stable binding (*SI Appendix*, Fig. S6B, Table S2). Unlike the model with maturation, these control models predicted a simple exponential increase in the number of Ndc80-CENP-T complexes followed by a k_{off}-dependent plateau (*SI Appendix*, Fig. S7E). Experimental results for complex formation and these theoretical predictions are plotted in Fig. 2E as broken and dotted lines. The experimental data align more closely with the predictions derived from the model with maturing sites.

Additionally, the model with maturation was used to predict results of experiments in which 1 nM CENP-T was incubated for 70 min with the range of Ndc80 concentrations (0-400 nM). The fraction of complexes was calculated for CENP-T^{2D}, CENP-T^{site1} and CENP-T^{site2} proteins in a mixture with 0-400 nM Ndc80 using 1 nM concentration step (Fig. 2F, solid lines). Theoretical curves for all proteins show a good match with the corresponding experimental curves (Fig. 2F, points) without any parameter adjustment.

Application of the model to describe results for soluble Ndc80 protein and immobilized CENP-T clusters.

CENP-T^{6D} clusters. The model for soluble Ndc80 protein and immobilized CENP-T^{6D} monomers was applied to experiments with immobilized CENP-T^{6D} clusters with 200 nM Ndc80 and 2, 10, 30, and 60 min interaction time (Fig. 3D). Same parameter values as listed in *SI Appendix*, Table S1 for CENP-T^{6D} monomers were used, however, the modeled curves provided a poor fit because the stable Ndc80 binding by clustered CENP-T was notably higher than that of the monomeric CENP-T for the same interaction time, whereas the dissociation and dissociation rates were similar. Therefore, the values of rate constants k_{on} , k_{off} and k^*_{off} were kept the same as for monomers, but the maturation rate constant k_{1mat} was increased by a factor of 2.5, and k_{2mat} was increased by a factor of 38 to provide a better match (*SI Appendix*, Fig. S11B,C, Table S1). This new set of constants also described well the concentration dependency obtained with immobilized CENP-T^{6D} clusters and 1-1,000 nM Ndc80 for 2 min interaction time (*SI Appendix*, Fig. S11D). Thus, the clustering of CENP-T specifically enhances the maturation rate, especially of site 2, and does not affect other kinetic constants.

Other CENP-T protein clusters. The model for soluble Ndc80 protein and immobilized CENP-T monomers and parameter values listed in *SI Appendix*, Table S2 for the corresponding CENP-T monomers was applied to experiments with immobilized CENP-T^{2D}, CENP-T^{site1} and CENP-T^{site2} clusters with 200 nM Ndc80 for 2 and 10 interaction time. Similarly to the CENP-T^{6D} clusters, a better fit was obtained when maturation rate constants were increased. Interestingly, the maturation rate constants k_{1mat} for clusters vary significantly between different proteins (Table S2), while k_{2mat} remains consistently fast. Thus, the maturation rate of site 1 appears to be sensitive to its immediate molecular environment and may be regulated at the kinetochore.

Table S1. Kinetic rate constants for interactions between Ndc80 and CENP-T^{6D} in different molecular forms.

All rate constants are listed in section "Reaction scheme and equations for Ndc80 and CENP-T interactions". Briefly, k_{on} - association rate constant for indicated site; k_{off} – dissociation rate constants for different sites and their states; k_{mat} – maturation rate constant for indicated sites; subscript 1 stands for site 1, subscript 2 for site 2, superscript * indicates constants for mature sites. The values listed in this table for CENP-T^{6D} monomers describe well our experimental results with both, the coverslip-immobilized and soluble CENP-T^{6D} protein.

rate constant	**site**	**units**	**CENP-T^{6D}**	
			monomers	clusters
k_{1on}	both nascent and mature site 1	10^{-3} nM^{-1}s^{-1}	2.5	2.5
k_{2on}	both nascent and mature site 2	10^{-3} nM^{-1}s^{-1}	2.5	2.5
k_{1off}	nascent site 1	10^{-5} s^{-1}	1,000	1,000
k_{2off}	nascent site 2	10^{-5} s^{-1}	1,000	1,000
k_{1off}^{*}	mature site 1	10^{-5} s^{-1}	5	5
k_{2off}^{*}	mature site 2	10^{-5} s^{-1}	5	5
k_{1mat}	maturation of site 1	10^{-4} s^{-1}	2	5
k_{2mat}	maturation of site 2	10^{-4} s^{-1}	8	300

Table S2. Kinetic rate constants for interactions between CENP-T mutant proteins and Ndc80

Abbreviations are the same as in Table S1. The same values of rate constants were used to model reactions involving coverslip-immobilized and soluble CENP-T monomers.

rate constant	**site**	**units**	**CENP-T^{2D}**		**CENP-T^{site1}**		**CENP-T^{site2}**	
			monomers	clusters	monomers	clusters	monomers	clusters
k_{1on}	both nascent and mature site 1	10^{-3} nM^{-1} s^{-1}	2.5	2.5	0.3	2.5	0	0
k_{2on}	both nascent and mature site 2	10^{-3} nM^{-1} s^{-1}	2.5	2.5	0	0	2.5	2.5
k_{1off}	nascent site 1	10^{-5} s^{-1}	1,000	1,000	1,000	1,000	0	0
k_{2off}	nascent site 2	10^{-5} s^{-1}	1,000	1,000	0	0	1,000	1,000
k^*_{1off}	mature site 1	10^{-5} s^{-1}	5	5	5	5	0	0
k^*_{2off}	mature site 2	10^{-5} s^{-1}	5	5	0	0	5	5
k_{1mat}		10^{-4} s^{-1}	2	20	1	6	0	0
k_{2mat}		10^{-4} s^{-1}	8	300	0	0	5	300

Supporting Figures and Legends

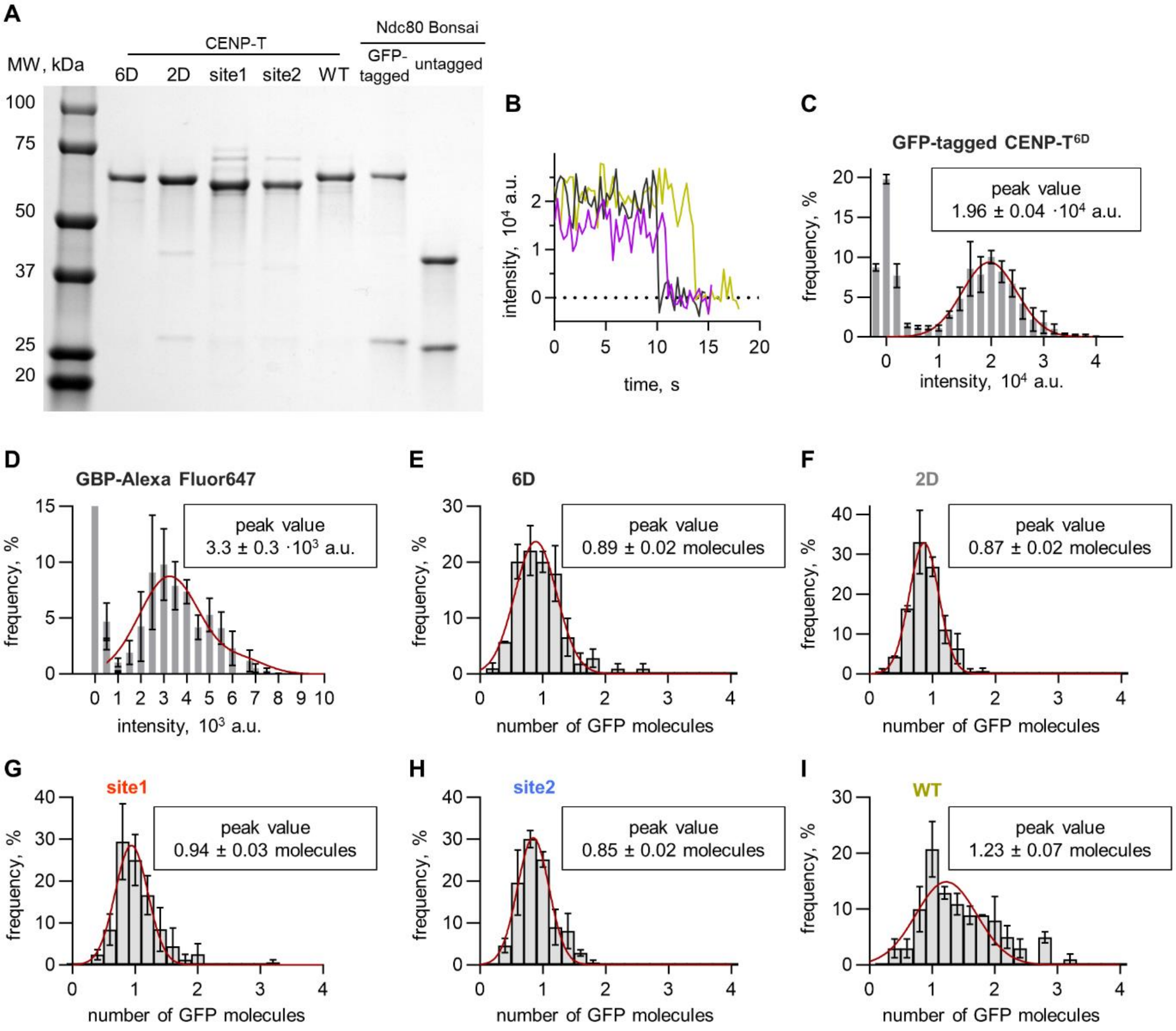

Fig. S1. Quantification of molecular brightness of isolated GFP-tagged proteins.

(A) Purified CENP-T and Ndc80 constructs used in this study were analyzed by SDS-PAGE. **(B)** Example photobleaching curves for GFP-tagged CENP-T^{6D} **(C, D)** Histograms of integral intensities collected from photobleaching curves. Binned data are represented with mean ± SEM, red lines are fittings of the main distributions with Gaussian functions. Peaks of intensities close to zero represent the background values. Panel (C) shows integral intensities of GFP fluorophore, number of independent experiments (N) = 3, total number of analyzed dots (n) = 47. Panel (D) shows integral intensities of Alexa Fluor 647 dye, N = 4, n = 112. **(E-I)** Histograms of the number of GFP molecules per fluorescent dot in the chamber with indicated GFP-tagged CENP-T construct, N = 3, n > 100 per protein. Values indicated on the graphs correspond to the peak value determined with Gaussian fitting and represent the number of CENP-T molecules per dot. Dots with several GFP molecules are rare and likely represent two or more molecules localizing close together.

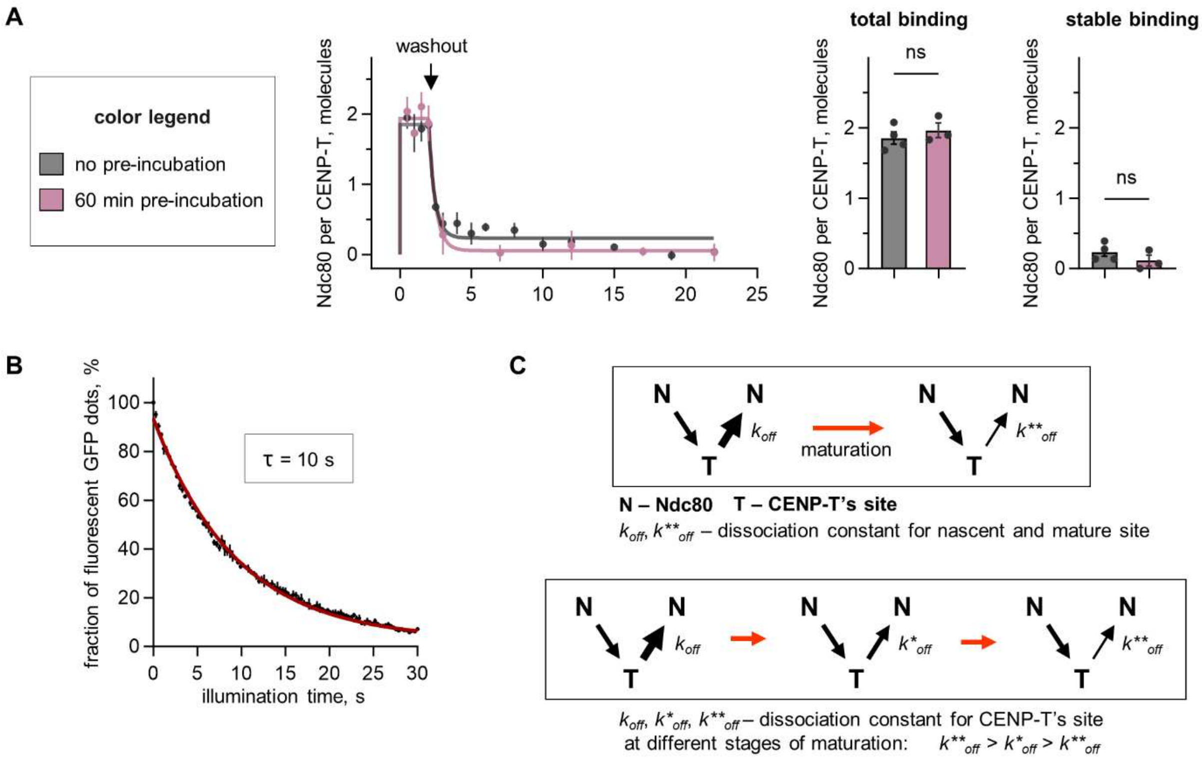

Fig. S2. Exchange of Ndc80 molecules on immobilized CENP-T^{6D} monomers.

(A) Left: number of Ndc80s bound per coverslip-immobilized CENP-T^{6D} monomer, as function of time. Soluble Ndc80 (200 nM) was added at time 0, immediately after immobilization of CENP-T^{6D} molecules (no pre-incubation, grey) or after 60 min pre-incubation of immobilized CENP-T^{6D} molecules on the coverslip (60 min pre-incubation, pink). At time point 2 min, Ndc80 was washed out. Each point is mean ± SEM, N = 3-4; lines are exponential fittings. Middle and right graphs show total and stable binding. Each point represents median from independent experiment, and the bars indicate their mean ± SEM. For all graphs, the default statistical test employed was the unpaired t-test with Welch's correction unless otherwise specified: not significant (ns) corresponds to $p > 0.05$, * to $p < 0.05$, ** to $p < 0.01$, *** to $p < 0.001$, and **** to $p < 0.0001$. Data for CENP-T^{6D} without pre-incubation are the same as in Fig. 1F. **(B)** Fraction of fluorescent GFP-tagged CENP-T^{6D} dots as a function of illumination time. The fraction was calculated as a number of fluorescent dots at the indicated time point normalized on an initial number of fluorescent dots. Each point represents the mean ± SEM from N = 3. Data were fitted to an exponential decay function to determine characteristic bleaching time (τ). **(C)** The diagrams of possible molecular pathways to explain site maturation. Different size of arrows symbolizes different reaction rates. Top: single-step transition reduces the dissociation rate constant, leading to biphasic dissociation. Bottom: the same result is achieved through a series of transitions, leading to more complex dissociation kinetics.

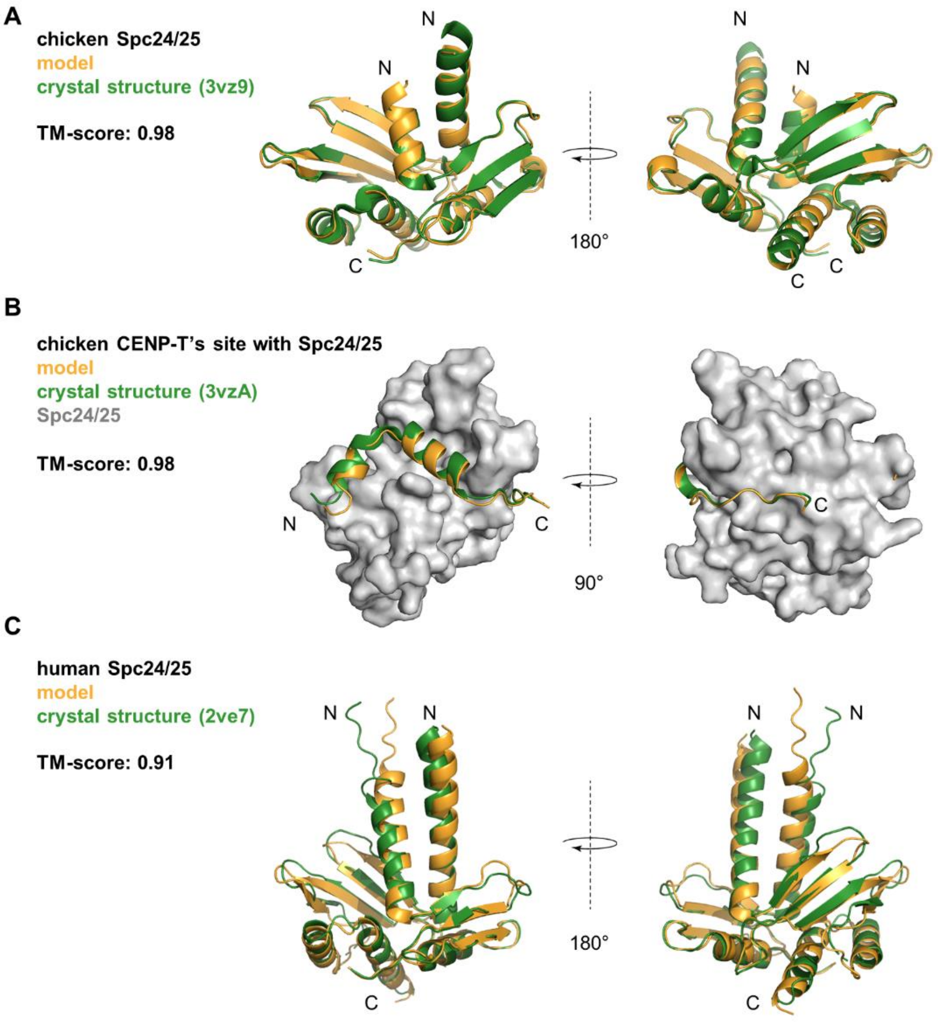

Fig. S3. Structural analyses using AlphaFold2.

(A) The crystal structure of chicken Spc24(134-195 aa)/Spc25(134-232 aa) complex obtained in (18) (PDB: 3vz9) is aligned with the structure of the same proteins predicted by AlphaFold2. **(B)** Crystal structure of chicken Spc24(134-195aa)/Spc25(134-232 aa) in complex with phosphomimetic CENP-T (63-93 aa; T72D, S88D) obtained in (18) (PDB: 3vza) is aligned with the structure of the same proteins predicted by AlphaFold2. **(C)** Crystal structure of human Spc24(122-197 aa)/Spc25(118-224 aa) obtained in (19) (PDB: 2ve7) is aligned with the structure of the same proteins predicted by AlphaFold2.

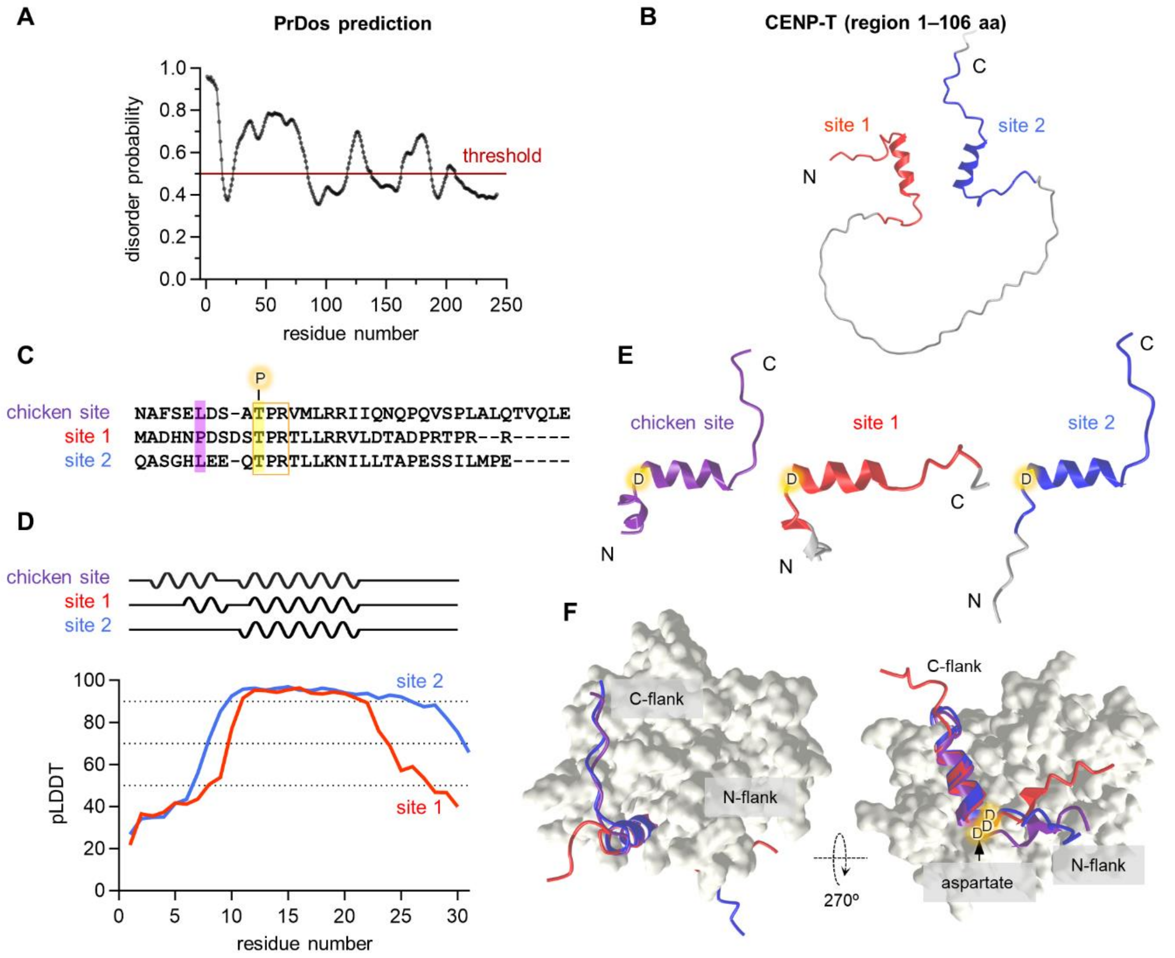

Fig. S4. Structural analysis of human CENP-T binding to Spc24/25 head.

(A) Disorder probability of CENP-T N-terminal region (1-242 aa) as predicted by PrDOS software (27). Amino acids with a disorder probability above 0.5 are expected to be disordered with false positive rate 5%. **(B)** Structure of N-terminal region of CENP-T (1-110 aa) as predicted by AlphaFold2 (16). Regions corresponding to site 1 (1-30 aa) are shown in red, and for site 2 (76-106 aa) – in blue. **(C)** Aligned sequences of chicken CENP-T's site (63-93 aa), human CENP-T site 1 (1-30 aa) and site 2 (76-106 aa). Within the sequences, essential leucine and its proline replacement in site 1 are highlighted in magenta; orange box shows Cdk phosphorylation site, the phosphorylatable threonine is highlighted in yellow. **(D)** Top: schematics of secondary structure of various CENP-T peptides: chicken peptide CENP-T was taken from crystal structure 3VZA (18); human CENP-T site 1 with phosphomimetic T11D substitution and site 2 with T85D was modeled in complex with Spc24(136-197 aa)/Spc25(127-224 aa) using AlphaFold2. Wavy lines show helical regions, and straight line shows unstructured regions. Bottom: local Distance Difference Test scores (pLDDT) predicted with AlphaFold2 for human site 1 and site 2. Horizontal lines demarcate confidence levels: < 50 represents very low confidence, 50-70 indicates low confidence, 70-90 is considered well-predicted, > 90 represents high confidence. **(E)** The structure of CENP-T's peptides is described in (D). **(F)** An alignment of human phosphomimetic site 1 and site 2 in complex with Spc24/25 (shown in grey) predicted by AlphaFold2 (see Fig. 2A for more details) and crystal structure of chicken CENP-T's site (3VZA (18).

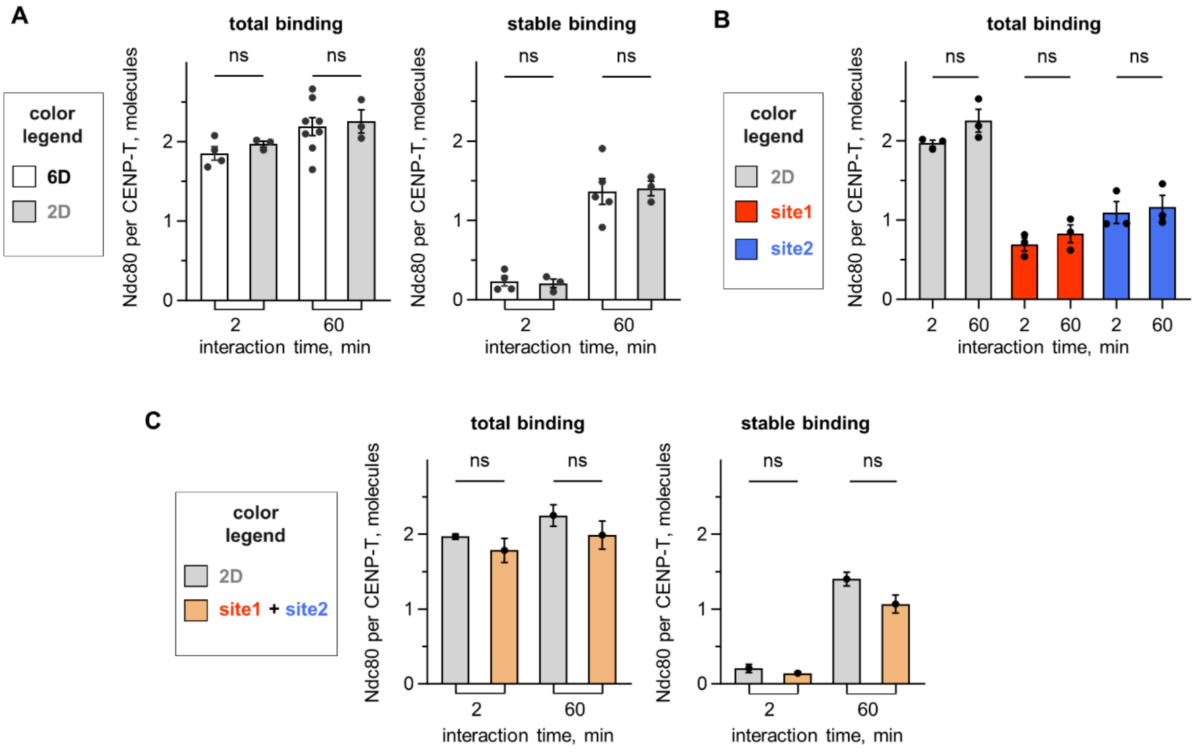

Fig. S5. Binding of Ndc80 to monomeric molecules of different CENP-T proteins.

(A) Total and stable binding of GFP-tagged Ndc80 to CENP-T^{6D} and CENP-T^{2D} monomers after 2 or 60 min of interaction with Ndc80 at 200 nM. Here and for other panels on this figure, each point represents an independent experiment (N = 3-8), and the bars indicate their mean ± SEM. Data for CENP-T^{6D} are the same as in Fig. 1G, and stable binding for CENP-T^{2D} are the same as in Fig. 2D, shown here for a direct comparison. **(B)** Total binding of Ndc80 to indicated CENP-Ts. **(C)** Total and stable binding of Ndc80 to CENP-T^{2D} monomers is plotted together with the arithmetic sum of analogous bindings to CENP-T^{site1} and CENP-T^{site2} monomers, as calculated based on data for these proteins on panel (B) and Fig. 2D. Error bar for the sum was calculated based on SEM errors of binding levels for CENP-T^{site1} and CENP-T^{site2}.

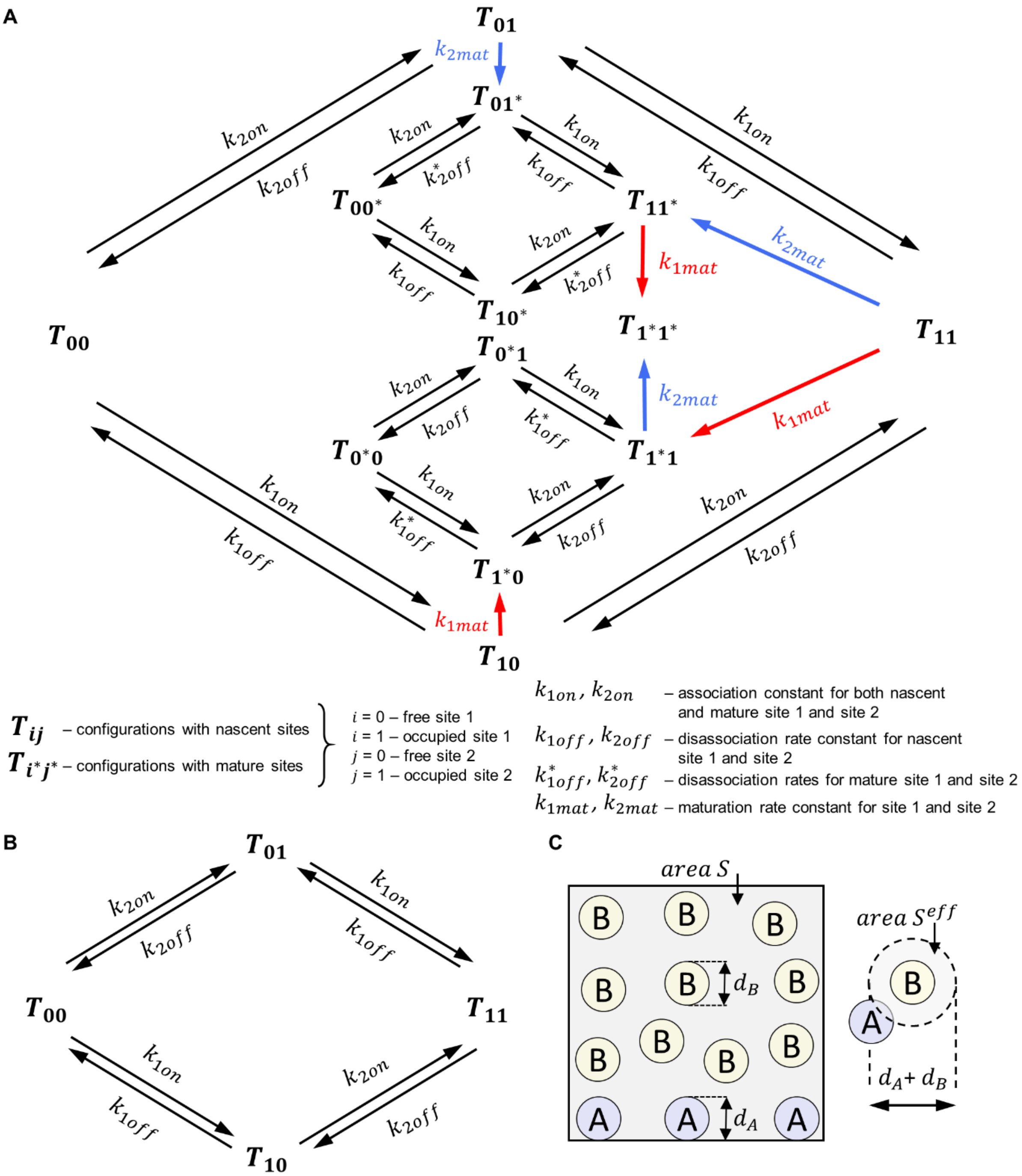

Fig. S6. Mathematical modeling of Ndc80 interaction with CENP-T sites.

(A) The reaction scheme illustrating the kinetic interactions between CENP-T (T) and Ndc80 (N) in our mathematical model. The outer contour represents the initial binding and unbinding of Ndc80 molecules to nascent sites on CENP-T. The red and blue arrows indicate the maturation of Ndc80 binding sites, leading to a switch to the inner contour, representing the binding of Ndc80 to mature sites, indicated as *. **(B)** The reaction scheme outlining the kinetic interactions between CENP-T and Ndc80, similar to panel (A), but excluding the maturation of CENP-T's sites. **(C)** Schematic illustration of interaction between molecules of reactant *A* (diameter d_A) attached to the chamber surface *S* and molecules of reactant *B* (diameter d_B) dissolved in the solution.

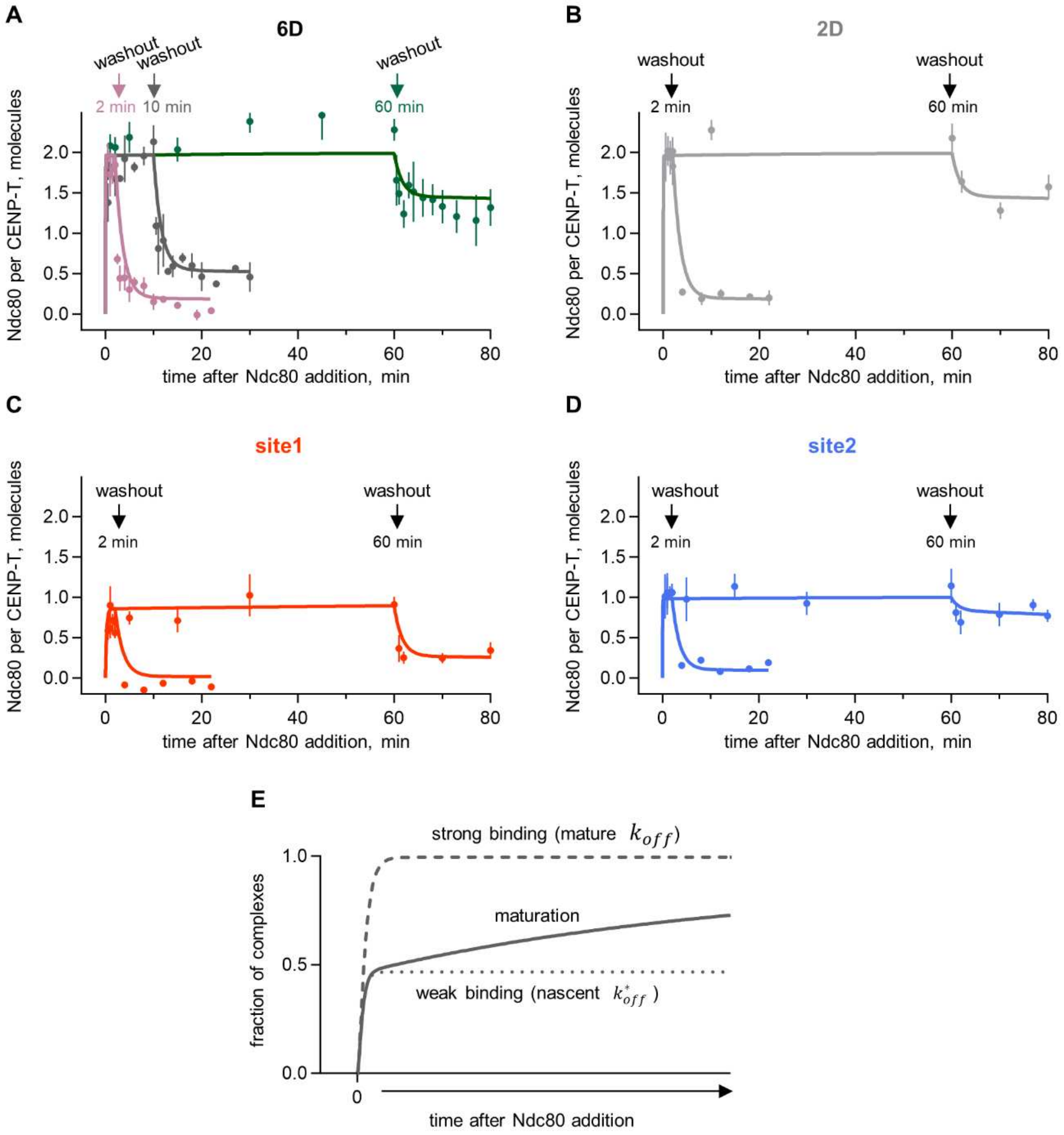

Fig. S7. Application of the mathematical model to Ndc80 interaction with monomeric CENP-T.

(A-D) Kinetics of Ndc80 interaction with different CENP-T monomers: dots are experimental points from Figs. 1F and 2C. Lines are model predictions. **(E)** Model predictions for the fraction of CENP-T^{2D} complexes with Ndc80 over time were calculated using constants in *SI Appendix*, Table S2 and 10 nM Ndc80.

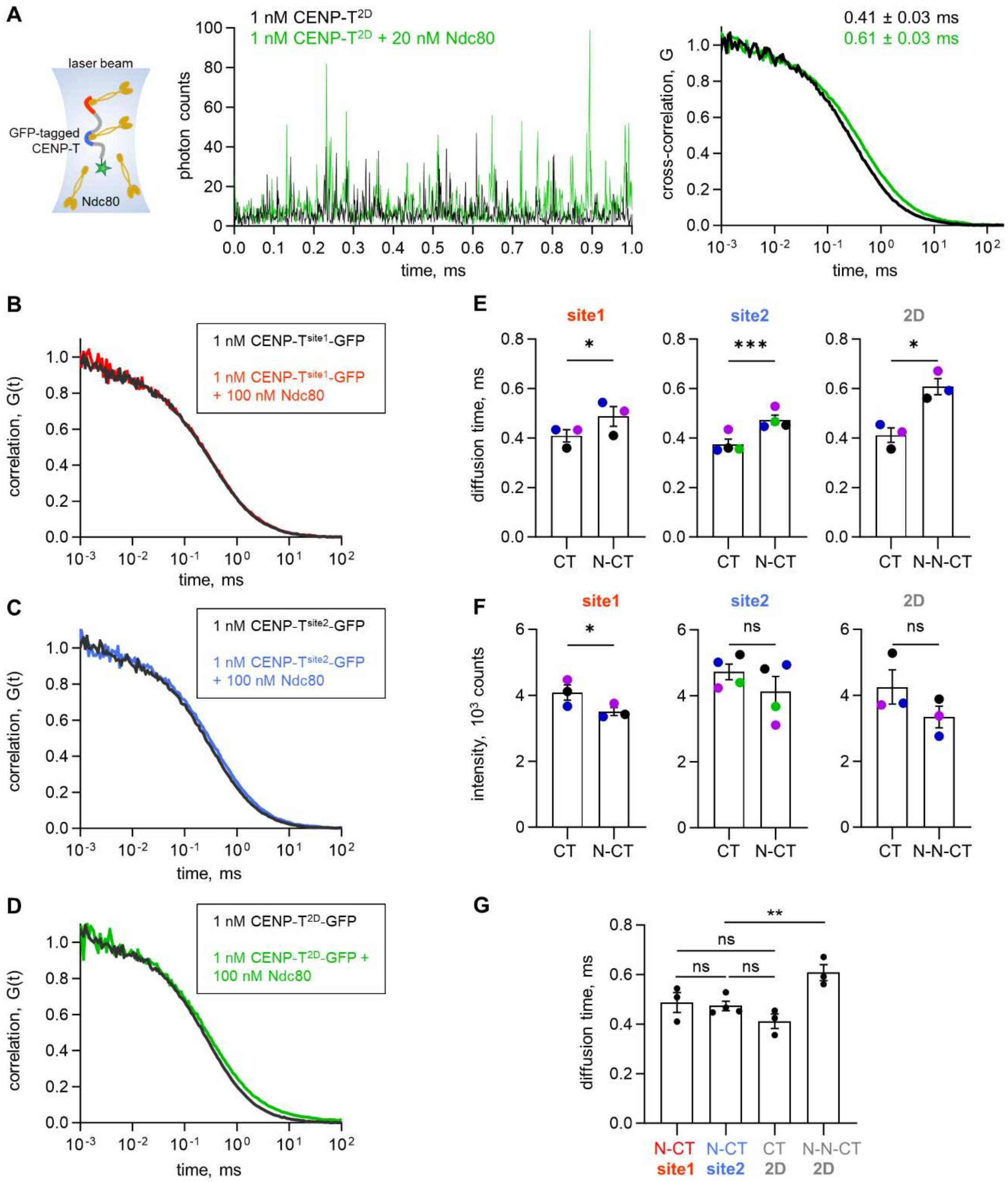

Fig. S8. Analysis of Ndc80 interactions with CENP-T using FCS approach.

(A) Scheme of FCS assay, example time traces, and corresponding cross-correlation curves for 1 nM GFP-tagged CENP-T^{2D} alone or with 20 nM unlabeled Ndc80. Shift between the cross-correlation curves indicates a change in diffusion time due to complex formation. Corresponding diffusion time values are indicated above the graph. **(B)**-**(D)** Example cross-correlation curves for indicated GFP-tagged CENP-T constructs alone or in the presence of 100 nM unlabeled Ndc80. **(E)** The diffusion time and **(F)** fluorescence intensity of the indicated CENP-T (CT) proteins alone or in a complex with one or two Ndc80 molecules (N-CT and N-N-CT). Each point represents an independent experiment, and points of the same color represent experiments carried out at the same time. Here, statistical significance was determined with a paired t-test. **(G)** Diffusion times of indicated CENP-T complexes alone, with one or two (2x) Ndc80 molecules.

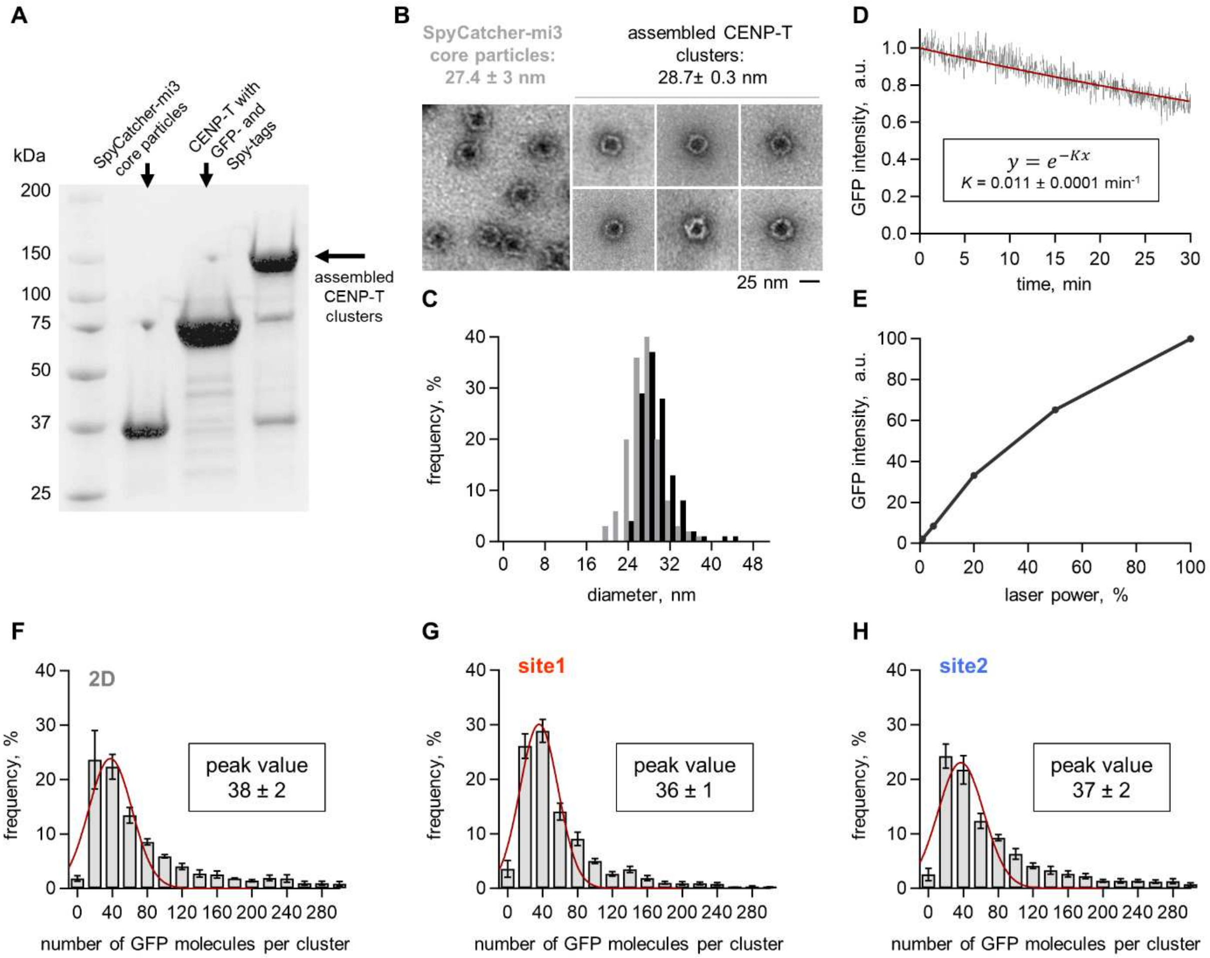

Fig. S9. Conjugation of different CENP-T constructs to mi3 core particle.

(A) Conjugation of 2.5 µM CENP-T with GFP- and Spy-tags to 5 µM SpyCatcher-mi3 core particles visualized using SDS-PAGE. **(B)** Example images of SpyCatcher-mi3 core particles before and after conjugation to CENP-T visualized by electron microscopy after negative staining. **(C)** The histogram of the diameter of SpyCatcher-mi3 core particles before (grey columns) and after conjugation to CENP-T (black columns). Graph is based on n = 140 SpyCatcher-mi3 core particles from N = 4 experiments, and n = 120 assembled CENP-T clusters from N = 3 experiments. **(D)** The photobleaching curve of the GFP-fluorophore on CENP-T clusters. Intensity values were normalized to their initial values, averaged, and then fitted with an exponential decay to generate the photobleaching curve. Each point represents the mean ± SEM from N = 3. **(E)** The calibration curve showing the normalized intensity of GFP-tagged CENP-T clusters at various laser power settings. Each point represents the mean ± SEM, N = 3. **(F)-(H)** Histograms of the number of GFP molecules per cluster for indicated GFP-tagged CENP-T protein. Binned data are represented with mean ± SEM, N = 5-6, n > 1,000 per protein. Values indicated on the graphs correspond to the peak value determined with Gaussian fitting (red line) and represent the number of CENP-T molecules per cluster.

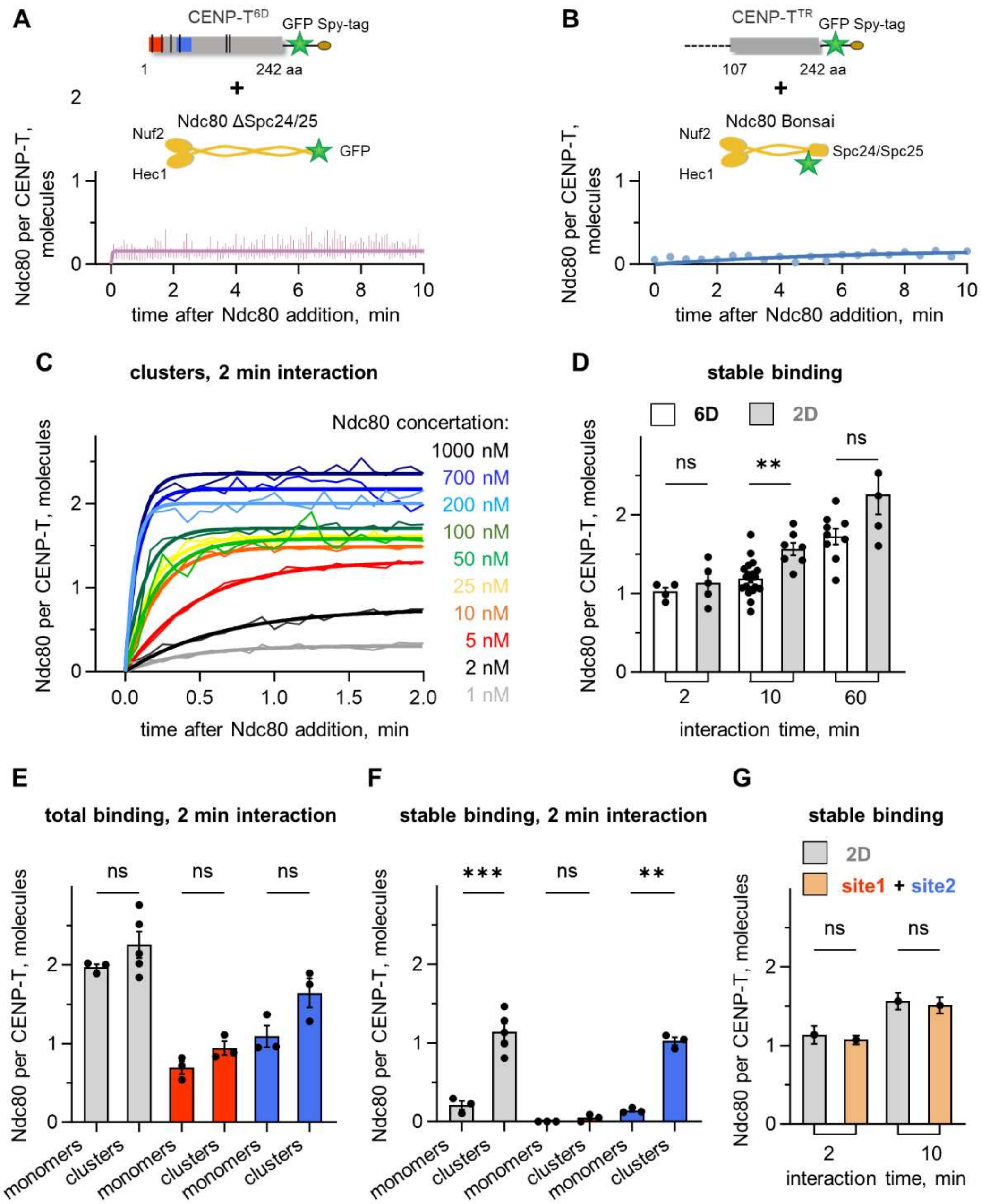

Fig. S10. TIRF-based assay to measure Ndc80 binding to clustered CENP-T.

(A) Number of Ndc80 ΔSpc24/25 molecules bound per clustered CENP-T^{6D}. Proteins are schematized above the graph to emphasize that Ndc80 ΔSpc24/25 protein lacks the CENP-T binding domain (Spc24/25 head). In panels (A) and (B) each point represents the mean ± SEM, N = 2-24. Lines in (A)-(C) are exponential fits. In panels (A), (B), (D)-(G), the concentration of Ndc80 is 200 nM. **(B)** Number of Ndc80 Bonsai molecules bound per clustered CENP-T^{TR}. The diagram illustrates the structure of the CENP-T^{TR} construct lacking the Ndc80 binding region 1-106 aa and the Ndc80 Bonsai construct. **(C)** Example time courses for Ndc80 binding with CENP-T^{6D} clusters at different concentrations of Ndc80. Each curve represents the binding in independent experiment with n > 23 clusters. **(D)** Stable binding of Ndc80 to clusters of CENP-T^{6D} and CENP-T^{2D}. The interaction time was controlled by washing out unbound Ndc80 molecules either 2, 10 or 60 minutes after the introduction of Ndc80 to the microscopic chamber. In panels (D)-(G), each point represents an independent experiment, and the bars indicate the mean ± SEM. **(E)** Total and **(F)** stable binding of Ndc80 to indicated CENP-Ts present on either monomeric or clustered form. **(G)** The stable binding of Ndc80 to CENP-T^{2D} clusters is plotted together with the arithmetic sum of analogous bindings to CENP-T^{site1} and CENP-T^{site2} clusters, as calculated based on data for these proteins in Fig. 3H. Error bars for the sum were calculated based on SEM errors of binding levels for CENP-T^{site1} and CENP-T^{site2}.

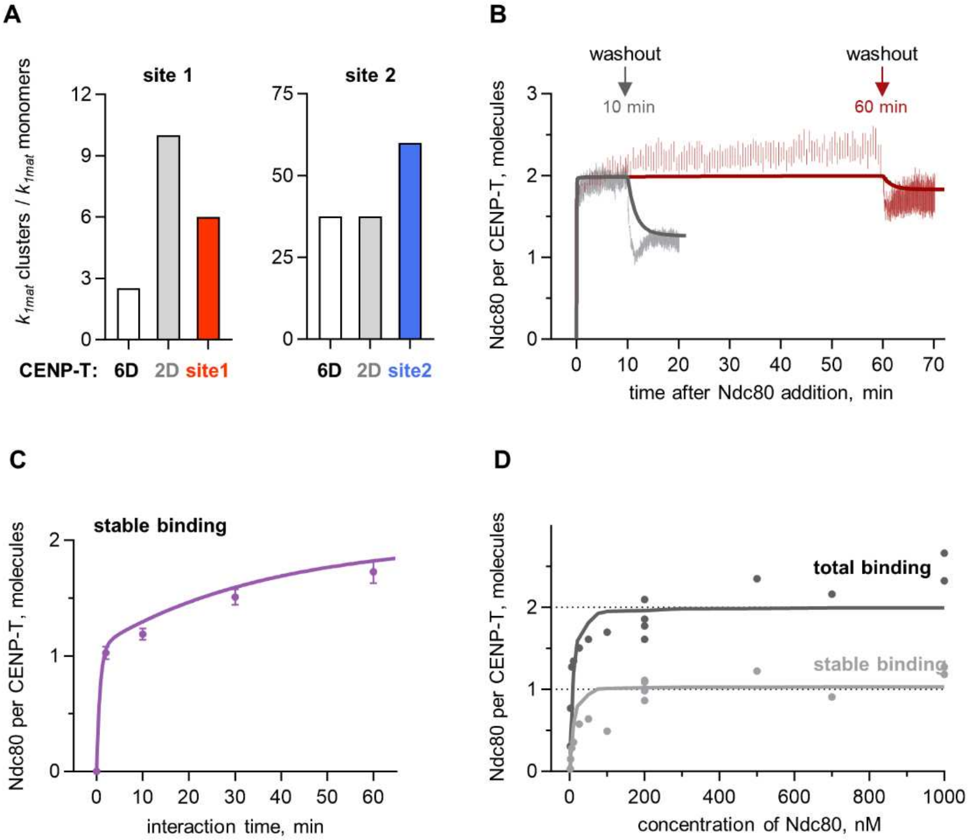

Fig. S11. Kinetic model of Ndc80 binding to clustered CENP-T.

(A) Enhancement of maturation rate of CENP-T site 1 and site 2 upon clustering of indicated CENP-T constructs. The acceleration in maturation rate is quantified as the ratio between maturation rates in monomers and clusters, as determined through a mathematical model. **(B)** The graph shows the number of Ndc80 molecules bound per CENP-T^{6D} molecule within the cluster as a function of time after the addition of Ndc80. Experiments shown here were done with a constant flow of 30 µl min^{-1} of 200 nM Ndc80 during the binding phase. Each point represents the mean ± SEM from N = 3-4. Here and below the lines connecting the experimental data points represent the corresponding predictions generated by the model. **(C)** A number of Ndc80 molecules bound stably per one CENP-T^{6D} molecule within the cluster (same as in Fig. 3F). **(D)** The total binding and number of stably bound Ndc80 molecules per one CENP-T^{6D} molecule within the cluster as function of Ndc80 concentration. In these experiments interaction time was 2 minutes, the experimental points are the same as in Fig. 3E.

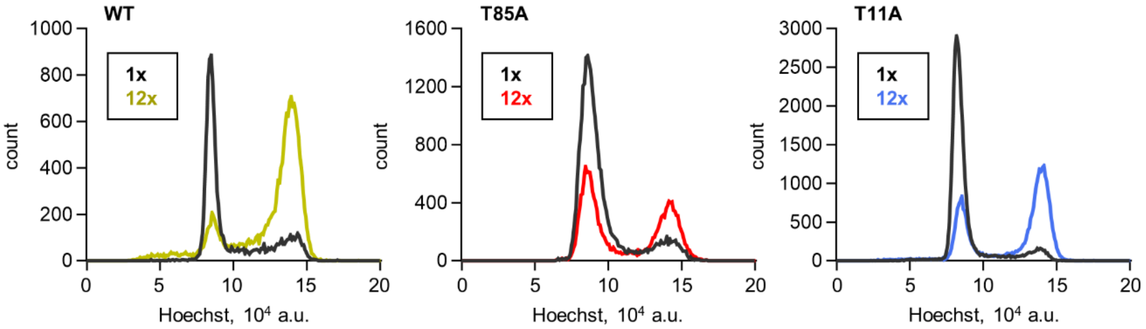

Fig. S12. Distribution of DNA content in cells expressing SunTag-based CENP-T oligomers.

Histograms showing the distribution of DNA content stained with Hoechst in HeLa cells expressing the indicated CENP-T constructs, which are either monomeric (1x) or oligomerized using the SunTag system into 12x-oligomers.

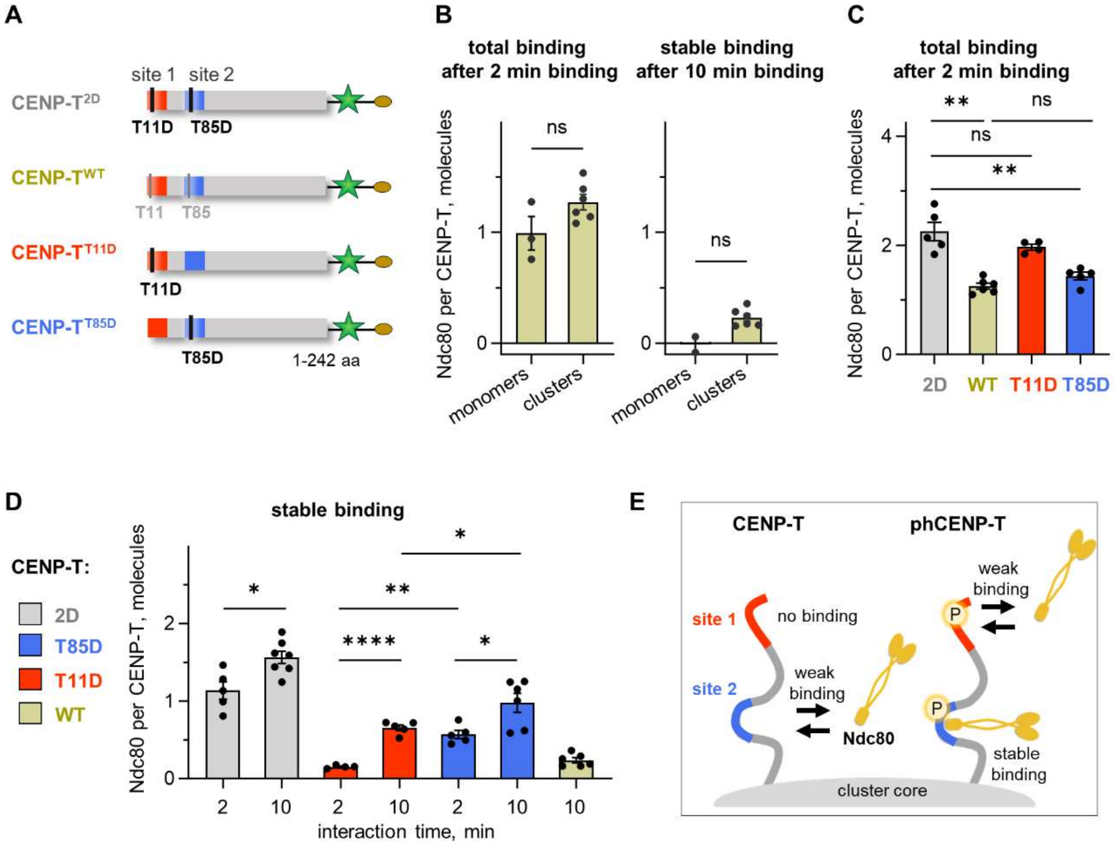

Fig. S13. Ndc80 binding to CENP-T's sites lacking phosphorylation.

(A) Diagram of the CENP-T^{2D} (2D), CENP-T^{WT} (WT), CENP-T^{T11D} (T11D), and CENP-T^{T85D} (T85D) constructs. **(B)** Comparison of total and stable Ndc80 binding monomeric and clustered CENP-T^{WT}. In panels (B)-(D) concertation of Ndc80 is 200 nM, each point represents an independent experiment, and the bars indicate the mean ± SEM. **(C)** Total Ndc80 binding to clusters of indicated CENP-T constructs after 2 min interaction. **(D)** Comparison of stable Ndc80 binding to clusters of indicated CENP-T constructs after 2 and 10 min interaction.

Movie S1 (separate file). Structure of human Spc24/25 head with bound peptides corresponding to the CENP-T sites.

Structures were predicted using AlphaFold2 software. Human Spc24/25 head composed of Spc24 (134-195 aa) and Spc25 (118-224 aa) is shown in grey; CENP-T site 1 (1-30 aa) is red, and site 2 (76-106 aa) is blue. The phosphomimetic substitutions T11D and T85D in site 1 and 2, respectively, are shown in yellow. The different extent of site 1 and site 2 wrapping around the Spc24/25 head is evident. Site 1 primarily establishes interactions with Spc24/25 through its central α-helix, whereas site 2 appears to form tri-partite interface encompassing the central α-helix and two adjoining flanking regions.

SI References

1. K. E. Gascoigne *et al.*, Induced ectopic kinetochore assembly bypasses the requirement for CENP-A nucleosomes. *Cell* **145**, 410-422 (2011).
2. N. Gudimchuk *et al.*, Probing Mitotic CENP-E Kinesin with the Tethered Cargo Motion Assay and Laser Tweezers. *Biophys J* **114**, 2640-2652 (2018).
3. K. Qian *et al.*, A simple and efficient system for regulating gene expression in human pluripotent stem cells and derivatives. *Stem Cells* **32**, 1230-1238 (2014).
4. L. Cong *et al.*, Multiplex genome engineering using CRISPR/Cas systems. *Science* **339**, 819-823 (2013).
5. T. Wang *et al.*, Identification and characterization of essential genes in the human genome. *Science* **350**, 1096-1101 (2015).
6. J. C. Schmidt *et al.*, The kinetochore-bound Ska1 complex tracks depolymerizing microtubules and binds to curved protofilaments. *Dev Cell* **23**, 968-980 (2012).
7. J. Schindelin *et al.*, Fiji: an open-source platform for biological-image analysis. *Nat Methods* **9**, 676-682 (2012).
8. D. R. Stirling *et al.*, CellProfiler 4: improvements in speed, utility and usability. *BMC Bioinformatics* **22**, 433 (2021).
9. C. McQuin *et al.*, CellProfiler 3.0: Next-generation image processing for biology. *PLoS Biol* **16**, e2005970 (2018).
10. A. V. Zaytsev *et al.*, Multisite phosphorylation of the NDC80 complex gradually tunes its microtubule-binding affinity. *Mol Biol Cell* **26**, 1829-1844 (2015).
11. T. U. J. Bruun, A. C. Andersson, S. J. Draper, M. Howarth, Engineering a Rugged Nanoscaffold To Enhance Plug-and-Display Vaccination. *ACS Nano* **12**, 8855-8866 (2018).
12. M. Chakraborty, E. V. Tarasovetc, E. L. Grishchuk, In vitro reconstitution of lateral to end-on conversion of kinetochore-microtubule attachments. *Methods Cell Biol* **144**, 307-327 (2018).
13. V. A. Volkov, A. V. Zaytsev, E. L. Grishchuk, Preparation of segmented microtubules to study motions driven by the disassembling microtubule ends. *J Vis Exp* 10.3791/51150 (2014).
14. G. B. Sissoko, E. V. Tarasovetc, O. Marescal, E. L. Grishchuk, I. M. Cheeseman, Higher-order protein assembly controls kinetochore formation. *Nature cell biology* 10.1038/s41556-023-01313-7 (2024).
15. Y. Chen, J. D. Müller, Q. Ruan, E. Gratton, Molecular Brightness Characterization of EGFP In Vivo by Fluorescence Fluctuation Spectroscopy. *Biophysical Journal* **82**, 133-144 (2002).
16. J. Jumper *et al.*, Highly accurate protein structure prediction with AlphaFold. *Nature* **596**, 583-589 (2021).
17. V. Hornak *et al.*, Comparison of multiple Amber force fields and development of improved protein backbone parameters. *Proteins* **65**, 712-725 (2006).
18. T. Nishino *et al.*, CENP-T provides a structural platform for outer kinetochore assembly. *EMBO J* **32**, 424-436 (2013).
19. C. Ciferri *et al.*, Implications for kinetochore-microtubule attachment from the structure of an engineered Ndc80 complex. *Cell* **133**, 427-439 (2008).
20. Y. Zhang, J. Skolnick, Scoring function for automated assessment of protein structure template quality. *Proteins* **57**, 702-710 (2004).
21. J. Xu, Y. Zhang, How significant is a protein structure similarity with TM-score = 0.5? *Bioinformatics* **26**, 889-895 (2010).
22. P. J. Huis In 't Veld *et al.*, Molecular basis of outer kinetochore assembly on CENP-T. *Elife* **5** (2016).
23. E. L. Elson, Fluorescence correlation spectroscopy: past, present, future. *Biophys J* **101**, 2855-2870 (2011).
24. A. J. W. G. Visser, M. A. Hink, New Perspectives of Fluorescence Correlation Spectroscopy. *Journal of Fluorescence* **9**, 81-87 (1999).
25. J. Widengren, R. Rigler, U. Mets, Triplet-state monitoring by fluorescence correlation spectroscopy. *J Fluoresc* **4**, 255-258 (1994).
26. F. Rago, K. E. Gascoigne, I. M. Cheeseman, Distinct organization and regulation of the outer kinetochore KMN network downstream of CENP-C and CENP-T. *Curr Biol* **25**, 671-677 (2015).

27. T. Ishida, K. Kinoshita, PrDOS: prediction of disordered protein regions from amino acid sequence. *Nucleic Acids Res* **35**, W460-464 (2007).